EUROPEAN
SPALLATION
SOURCE

Author:	**F. Belloni, F. Benedetti, J. Marroncle, C. Thomas**
Reviewer:	
CHESS:	ESS-0680909
Date:	February 3, 2019
Version:	0.2

Prototyping, design and test results of the cNPM

Contents

List of Figures

List of Tables

Introduction

Scope of the documents

CEA/IRFU is designing five non-invasive profile monitors (NPM) for the cryogenic part of the ESS Linac in the framework of the in kind contribution agreement. Cryogenic radio frequency cavities require a clean environment and a high vacuum around 10^{-9} mbar. At this level of pressure the signal detection becomes critical thus, the profile monitors will rely on the direct collection of the ionized particles from the vacuum residual gas (IPM) instead of the beam induced fluorescence (BIF or FPM for Fluorescence Profile Monitor).

Preliminary Design Review has pointed out that two kinds of ionization profile monitor may be considered with both advantages and drawbacks: **conductive strips** or **optical** ionization profile monitor. Principle of operation is almost the same except that readout is different. During the past two years these two types of ionization profile monitor have been designed and tested on a proton beam at Saclay.

The present document mainly focuses on several topics concerning the optical and the strips ionization profile monitor, including: global overview of the IPM, experimental setup and results from beam test campaigns and outlooks for the final version.

Abbreviation

Abbreviation	Explanation
BPM	Beam Position Monitor
E3	ESS EPICS Environment
EMVA	European Machine Vision Association
EPICS	Experimental Physics and Industrial Control System
FWHM	Full Width at Half Maximum
FPM	Fluorescence Profile Monitor
CSS	Control System Studio
CMOS	Complementary Metal Oxide Semiconductor
GigE	Gigabit Ethernet
IOC	Input/Output Controller
IPHI	Injecteur de Protons à Haute Intensité (High Intensity Protons Injector)
IPM	Ionization Profile Monitor
LEBT	Low Energy Beam Transport line
MCP	MicroChannel Plate or Multiple Channel Plate
MEBT	Medium Energy Beam Transport line
NPM	Non-invasive Profile Monitor
OPI	OPerator Interface
PoE	Power over Ethernet
PV	Process Variable
RFQ	Radio Frequency Quadrupole
RGA	Residual Gas Analyzer
SDK	Software Developer Kit

Chapter 1

Prototype overview

1.1 Ionization Profile Monitor

Ionization Profile Monitor (IPM) is a type of non-destructive detector that measures the transverse profile of a beam (NPM). Principle of operation is summarized in the Figure 1.1a or in few words, as follows. Protons from beam pass through the vacuum, inducing ionizations of the residual gas: electron/ion pairs are created. The profile is reconstructed in one transverse direction. For a complete profile a pair of IPM is mandatory. Inside the IPM, a strong electrical field drives electrons or ions towards a segmented readout plane. The profile is reconstructed in one transverse direction. For a complete profile a pair of IPM is mandatory. **A MicroChannel Plate and phosphorus screen are used as readout for the optical IPM** and **conductive strips in the case of the strips IPM**.

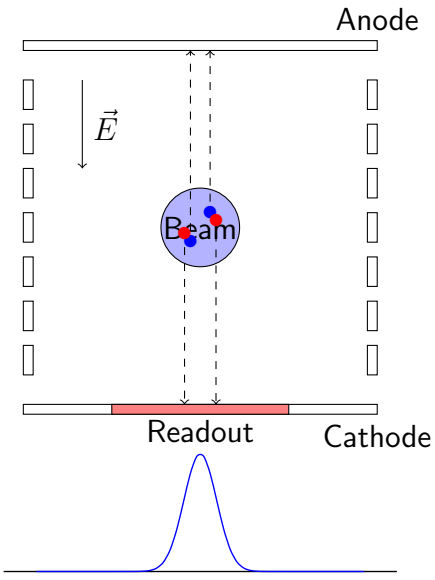

(a) How an IPM works. The electrical field can be reverted by inverting the polarity so it's possible to detect ions or electrons. Field correctors or degraders, on left and right, improve the field uniformity.

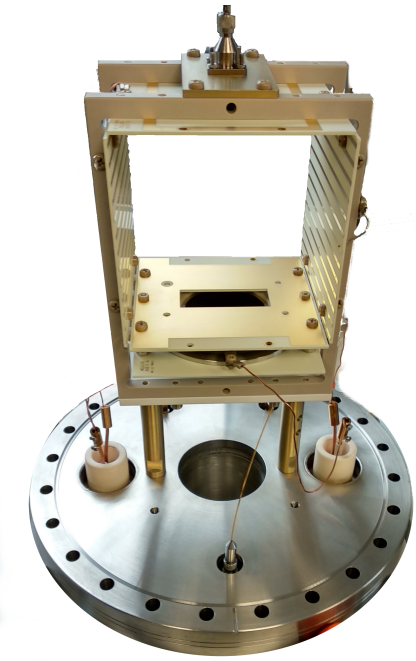

(b) An IPM Prototype. The readout is visible through the rectangular slit, here it is a MCP. Field correctors are also present on left and right plates.

Figure 1.1: A conceptual view of an IPM and its implementation.

1.2 Strips IPM

Two different strips detectors were used. One has 32 strips, 30 mm long and 0.8 mm wide, separated by 120 μm. This is what will be called throughout all this document "linear read-out", or "linear strips". Its layout is given in Table 1.1

STRIP NUMBER	x_min	x_max
1	-14.66	-13.86
2	-13.74	-12.94
3	-12.82	-12.02
4	-11.90	-11.10
5	-10.98	-10.18
6	-10.06	-9.26
7	-9.14	-8.34
8	-8.22	-7.42
9	-7.30	-6.50
10	-6.38	-5.58
11	-5.46	-4.66
12	-4.54	-3.74
13	-3.62	-2.82
14	-2.70	-1.90
15	-1.78	-0.98
16	-0.86	-0.06
17	0.06	0.86
18	0.98	1.78
19	1.90	2.70
20	2.82	3.62
21	3.74	4.54
22	4.66	5.46
23	5.58	6.38
24	6.50	7.30
25	7.42	8.22
26	8.34	9.14
27	9.26	10.06
28	10.18	10.98
29	11.10	11.90
30	12.02	12.82
31	12.94	13.74
32	13.86	14.66

Table 1.1: Linear detector geometry.

The second detector has 18 strips 30 mm long and variable width from 0.8 mm to 9 mm separated by 120 μm. This detector is reffered to as "gaussian strips" or "gaussian read-out" and its layout is given in Table 1.2[1].

[1]In such table the strip number starts from 1. As will be see in the section §1.6, for each read-out 32 channels are available (from 0 to 31). The gaussian strips are linked to the central channels, therefore strip 1 corresponds to channel 7, strip 2 to channel 8,...

STRIP NUMBER	x_min	x_max	width
1	-25.02	-16.02	9
2	-15.9	-10.9	5
3	-10.78	-7.78	3
4	-7.66	-5.66	2
5	-5.54	-4.04	1.5
6	-3.92	-2.92	1
7	-2.90	-1.90	0.9
8	-1.78	-0.98	0.8
9	-0.86	-0.06	0.8
10	0.06	0.86	0.8
11	0.98	1.78	0.8
12	1.9	2.8	0.9
13	2.92	3.92	1
14	4.04	5.54	1.5
15	5.66	7.66	2
16	7.78	10.78	3
17	10.9	15.9	5
18	16.02	25.02	9

Table 1.2: Gaussian detector geometry.

1.3 Optical IPM

1.3.1 MicroChannel Plate

A MicroChannel Plate (MCP) generates electrons from incident particles. It can be seen as a glass lead plate drilled with micro-metric tilted holes. A specific coating is applied on its input surface to increase secondary emissions. When a particle hits the MCP hole entrance then secondary electrons are emitted. Due to difference of potential, secondaries are drawn towards the channel output and strike hole walls again, creating more and more electrons. Then, electrons are collected on a detection plane that can be a single electrode, multiple electrodes or a phosphorus screen depending on the requirements (sensitivity, spatial and time resolution). Figure 1.2 presents some schematic representations of how an MCP works.

Gain or multiplication factor for a single MCP is about 10^2 to 10^4 depending on the V_{MCP} voltage, usually from 600 to 1000 V. MCP can be stacked to increase the gain to 10^6 or even more. Typical configurations are single stage, chevron stack (double stages) or Z stack (triple stages).

Unfortunately MCPs have some drawbacks. First one is the lifetime, indeed the coating is damaged by the incident particles thus the gain is not stable and decreases over the time. Second disadvantage is the MCP gain limitation due to saturation mode. If the incident particle flux is too high then holes may be saturated, and they cannot amplify anymore. When it happens to a channel then it takes some times to recover.

For the optical IPM, we use single stage MCPs with different types of phosphorus screen: P43 (slow, high sensibility) and P46 (fast, less sensible)[1]. We bought the MCPs from the two main MCP providers: Photonis[2] and Hamamatsu[3].

1.3.2 Vision System

A vision system is necessary to record light from the phosphorus screen. A camera with a lens should be sufficient in our case.

[2] https://www.photonis.com/product-lines
[3] https://www.hamamatsu.com/eu/en/index.html

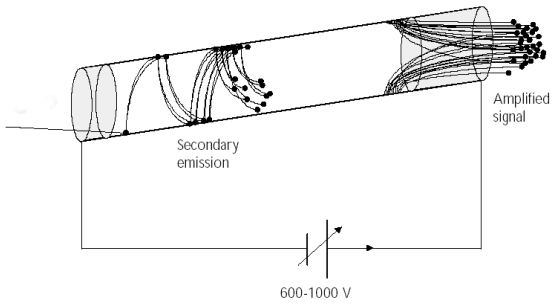

(a) A single MCP hole scheme. If an incident particle impacts a channel then it creates a kind of electron avalanche due to secondary emissions that occur in a MCP hole.

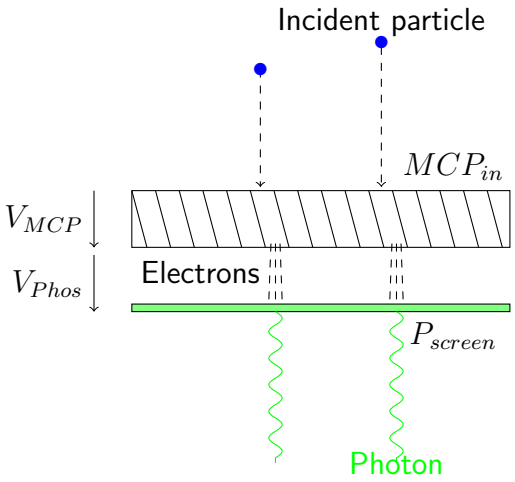

(b) A MCP with a phosphorus screen. Incident particles are converted to electrons and multiplied by the MCP. Then amplified electrons are converted to photons with a phosphorus screen.

Figure 1.2: Schematic views of how a MCP works.

Sensor is the core component of a camera so it's better to choose the sensor first with respect to the requirements. For our application high resolution is not mandatory, so pixels could be relatively big in order to increase light collection and dynamic range. Sony IMX249 fits well with these prerequisites. It's a consumer CMOS sensor with relatively big pixels and low noise. Its EMVA characteristics [2] are summarized in the Table 1.3.

Resolution	1936 (H) * 1216 (V)
Pixel size	5.86 μm
Sensor diagonal size	13.4 mm (Type 1/1.2)
Well capacity	32000 e-
Dynamic Range	70 dB
QE at 525 nm	70 %
Electrons noise	6.8 e^-
ADC	10 or 12 bits
Max framerate	30 fps

Table 1.3: Main features of the Sony IMX249 sensor

AlliedVision, Basler and FLIR propose several cameras based on the IMX249 sensor with different interfaces, features, form factors, prices and availability. We restricted our choice to GigE cameras since they allow long cable length and Power over Ethernet (PoE) which are quite useful features for an accelerator experiment. At the end we choose the FLIR Blackfly-PGE-23S6M-C[4].

The last step is the choice of a correct lens for the camera. Unfortunately lens suppliers doesn't provide full characteristics of their lenses, hence only the thin lens approximation has been considered. Distance from back of phosphorus screen to external air-side of viewport is 247mm. Active area radius of our MCPs is around 25mm thus

[4] https://eu.ptgrey.com/blackfly-23-mp-mono-gige-poe-sony-pregius-imx249-2

magnification, with respect to a sensor size of 11.34 mm, should be at least 0.2268. Table 1.4 shows magnification for several focal length. A focal length of 50 mm fits very well with our configuration.

Focal length (mm)	5	15	28	35	50	75	100	150
Magnification	0.02	0.069	0.127	0.165	0.255	0.436	0.68	1.546

Table 1.4: Magnification for several commom focal lengths, at working distance of 247mm

Lenses with 50mm focal length are rather standard and commercially available at moderate cost. In addition these lenses have a large numerical aperture (or small F-number) so they provide a large photon capture efficiency.

1.4 Power supply

An IPM requires high voltages to create the extraction field and to supply the MCP when it is used as readout. All power supplies come from iseg-HV[5] and cover the range from 0 kV to 30 kV with negative or positive polarity.

MCPs allow complete floating configuration. This means that the readout can work at very high potential. We refer this configuration as **symmetric** since the MCP is at the opposite value of the extracting electrode. In this case the electric field is more uniform if no corrections are applied (Figure 1.3d). However, it greatly increases the number of high voltage power supplies and the design complexity (Figure 1.3b). Of course MCPs work also correctly at ground (Figure 1.3a), we refer this set-up as **asymmetric**. In this configuration field correctors are mandatory[6] otherwise the uniformity is poor (see Figure 1.3c). During the two test campaigns we were able to work in both configuration. The strips IPM supports only the asymmetric configuration and does not require more than one high voltage.

[5] https://www.iseg-hv.com/en/products/detail/CPS

[6] See simulation results presented at the 4th BI Forum or Appendix D.

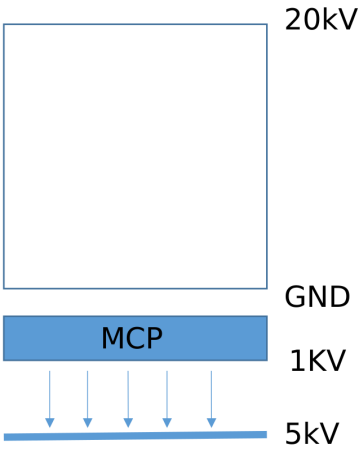

(a) Asymmetric configuration. Readout is grounded while extracting electrode is at certain potential.

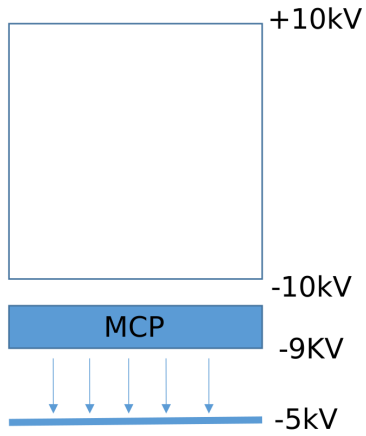

(b) Symmetric configuration. Readout and extracting electrode are at opposite potential.

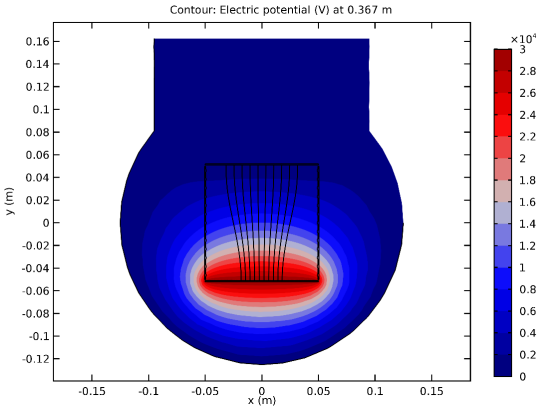

(c) Electrical field in asymmetric configuration. There is no field corrections applied here.

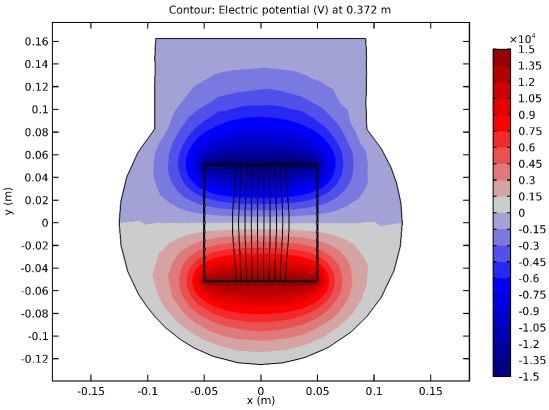

(d) Electrical field in symmetric configuration. There is no field corrections applied here.

Figure 1.3: Asymmetric or symmetric configuration, MCPs allow both.

1.5 Control System

The whole system[7] is almost fully compatible with EPICS toolkit[3], but we don't know exactly the level of compliance with E3. All applications were compiled with the version 3.16 of EPICS base. Three OPIs have been developed for the optical IPM in order to control cameras, power supplies and geobrick. They run under BOY module of the ESS Control System Studio (version 4.5.x).

Since all high voltage power supplies have their own SPCI Ethernet interface, thus a simple softIOC with asynDriver[4] and StreamDevice[5] was enough to control and monitor them.

Blackfly cameras from FLIR are fully compatible with three modules in areaDetector[6]: ADPointGrey, ADSpinnaker and aravisGigE. The ADPointGrey module uses a legacy SDK from FLIR, FlyCapture, thus it provides more features than other. On the other hand, FLIR recommends using the Spinnaker SDK for new development since the FlyCapture SDK will be deprecated. Another solution is to use aravisGigE which may be compatible with every GenICam compliant camera. We use also several areaDetector plugins to process the acquired images. The ADHDF5 plugin has been successfully used for packing and saving camera images together with some accelerator data. The ESS ADfit plugin has been also (somehow) tested with some limitations, see Result - Current section.

An Archiver Appliance[7] records and saves slow process variables from the power supplies, the vacuum systems and the accelerator.

Figure 1.4 shows the network architecture during the beam tests.

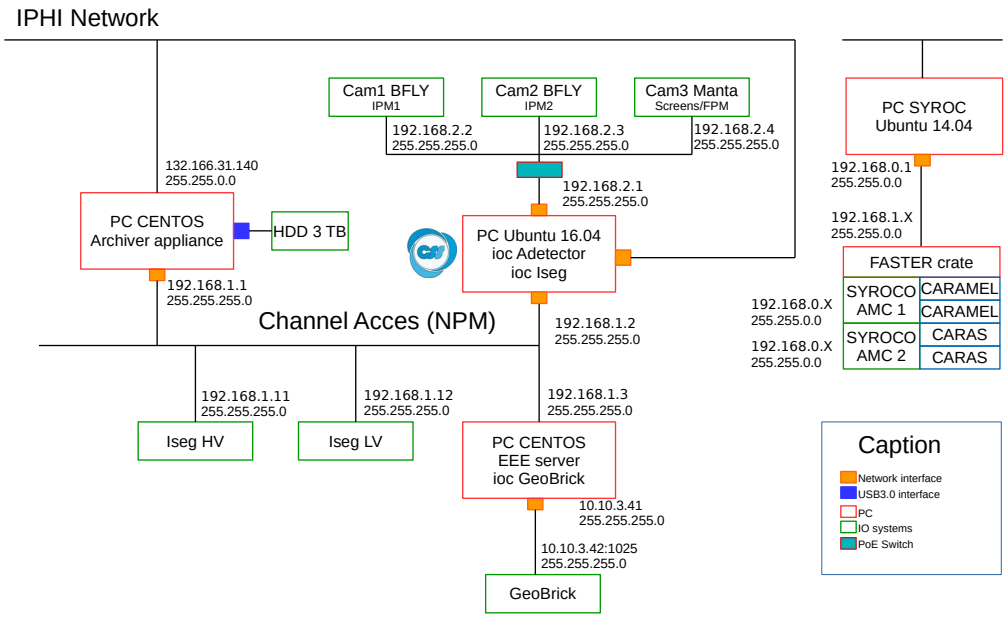

Figure 1.4: EPICS network setup during beam tests.

[7]The FASTER system is not integrated into our EPICS environment.

1.6 Electronics for the strip read-outs

As previously mentioned, the strip read-out is not integrated in the control system. The FASTER (Fast Acquisition System for nuclEar Researchs [8]) electronics was used to pre-process and save to computer the signals detected in the two strip read-outs. FASTER is a modular Acquisition system. Our set-up consisted of:

- 1 μTCA crate
- 1 motherboard $syroco\_amc\_c5$
- 2 daughterboards $caramel$
- 1 motherboard $syroco\_amc$
- 2 daughterboards $caras$ (of which only one was used)

To be able to see both positive and negative signals, an in-house manufactured offset box was also used to move the signal baseline towards positive values.

A scheme of the electronic chain is reported in fig. 1.5. Oversimplifying, the signal from each strip of the detector is added to the signal from the offset box. 32 signals exit from the offset box. In case of gaussian strips 6 channels (32-18 = 14) will show a signal equal to the box offset, since they are link to no strip (see § 1.2) and are sent to the caramel card. This daughterboard is equipped with 2 DDC316 chips [9] from Texas Instruments, each treating 16 channels. The treatment consists in a I-to-V integration. The integration time is adjustable from 10 μs to 1ms. The result of $\int Idt$ is therefore a charge. The output full scale is programmable (3 pC, 6 pC or 12 pC).

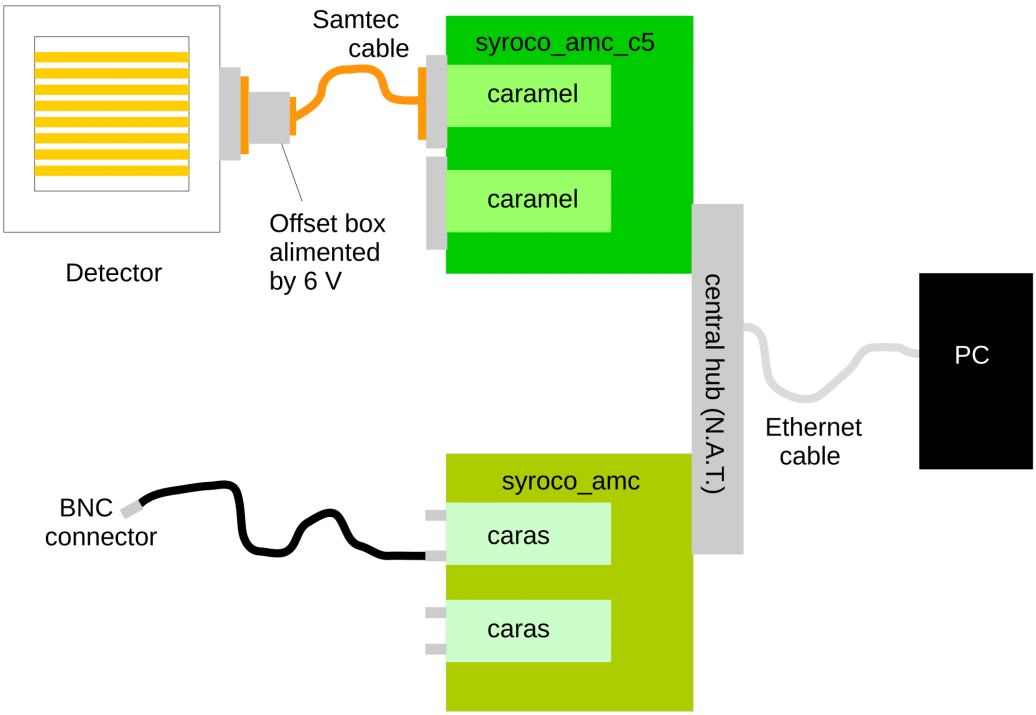

Figure 1.5: Scheme of the electronic chain.

1.7 Test bench

A test bench has been also developed in order to test the prototypes. The bench can be split into two different independent parts. The first part (upstream) tries to mimic the ESS LWU chamber on which two IPMs can be inserted. The idea is to be close to the ESS conditions in term of high voltages and electrical fields. The second part (downstream) offers one more IPM slot and two viewports for reference measurements in order to compare with the IPMs. Two solutions have been considered for the reference measurements, fluorescence profile monitor (FPM) and scintillating screens. The IPMs can be mounted independently in Y or X direction thanks to their design, thus it is even possible to measure the same profile direction with all three IPMs.

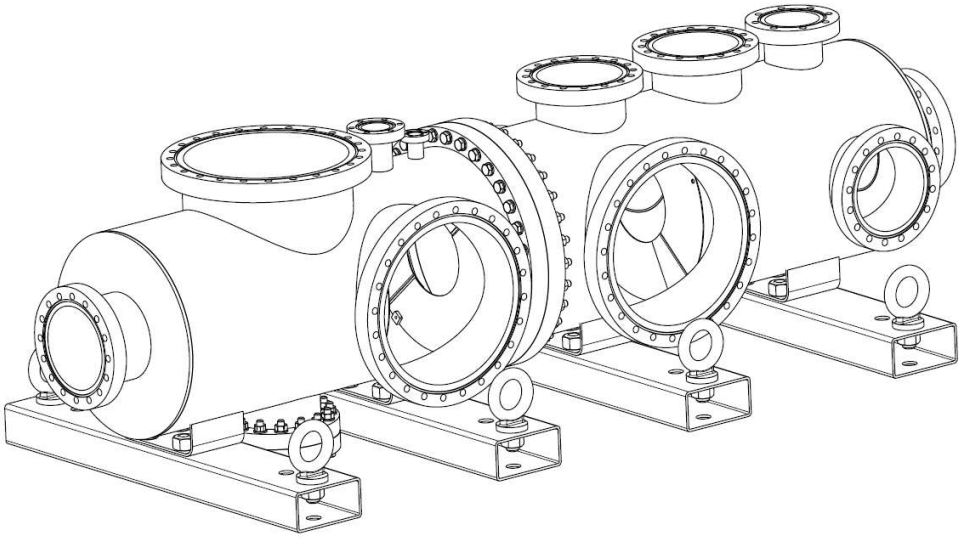

Figure 1.6: IPM test bench. Left part is the LWU-like vessel while right part add more viewports for testing purposes.

Chapter 2

Results from beam tests

2.1 L'Injecteur de Protons à Haute Intensité (IPHI)

IPHI is a high intensity linear proton accelerator located at CEA/Saclay. This project has been started in the late of 90's[10] but protons were accelerated up to 3 MeV in April 2016[11].

Proton plasma is created by an electron cyclotron resonance source (ECR), and transported toward a radio frequency quadruple (RFQ) by a low energy beam transport line (LEBT). An iris assures a fine tuning of the current, and two solenoids focus and filter the plasma before the injection in the RFQ. Then, the protons are accelerated up to 3 MeV and bunched with a frequency of 352 MHz by the RFQ. A medium energy beam transport line (MEBT), downstream from the RFQ, contains focusing elements, steerers, dipole magnet and beam diagnostics. The dipole magnet can distribute the protons over two beam lines.

The main line has a dedicated beam stop of 300 kW, allowing the commissioning of the accelerator at high intensity and duty cycle. The secondary line is more modular but restricted to lower intensity and duty cycle (few hundred Watts). This line is open for external user experiments. We were, with the nBLM team, one of the first experiments on the deviated line[12].

Figure 2.1 shows schematic view of IPHI accelerator, and Table 2.1 sums up difference between IPHI and ESS.

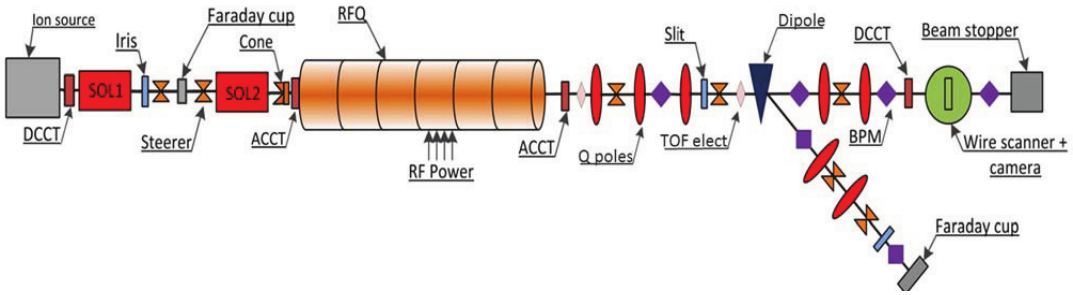

Figure 2.1: Schematic view of IPHI accelerator. The layout is almost up to date except that the slits have been removed. Our test bench was installed just after the last BPM on the deviated line. There is no profile measurement on this line.

	IPHI accelerator	ESS accelerator
Energy	3 MeV	2 GeV
Max current	100 mA	62.5 mA
Max pulse duration	up to DC	2.86 ms
Max pulse repetition	-	14 Hz
Vacuum range	$5 \cdot 10^{-7}$ to $1 \cdot 10^{-8}$ mbar	$1 \cdot 10^{-9}$ mbar

Table 2.1: Comparison between IPHI and ESS accelerators.

2.2 Test campaigns

We had the opportunity to test our prototypes at IPHI twice. Some pictures of the installation are shown in Figure 2.2.

(a) The test bench mounted on the deviated line of IPHI.

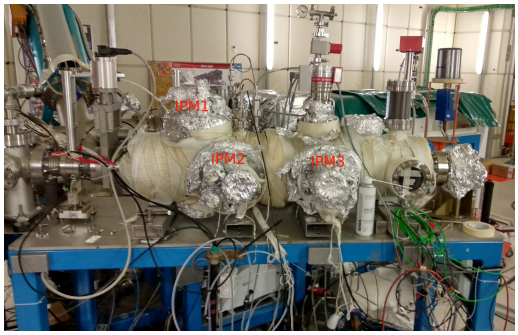

(b) Zoon on our IPM test bench. Three IPMs can be tested on this bench.

Figure 2.2: Installation of our test bench at IPHI.

In this section, we also want to introduce the story behind our two test campaigns, and give an overview of issues we faced. The prototypes were not ready for the beginning of the first campaign. Hence, they were debugged on site, and we encountered many technical problems (sparks, readout sync). We finally got our first profile after some fixes on our prototypes, and by reducing the maximum operating voltage. However, our prototypes were not able to measure the beam profile each day, and we observed strange artifacts on our profile. We solved this problem by asking a fine tuning of the beam parameters by a beam physicist. We became even more confident with our detectors when BPM systems were switched on, see next section.

Just after the first campaign we improved our detectors by minor changes on the HV connection design. Therefore, we decided to go for another time at IPHI. The second campaign confirmed and improved our first results. On the other hand, we didn't manage to perform all advanced tests we planed to do. The beam time was shared between four experiments, with each different requirements on the beam parameters. Unfortunately, the schedule was not respected due to technical problems and other external reasons, so we had to manage our tests daily and get along with the other experiments.

The Table 2.2 summarizes our two beam test campaigns, and more details are available in the Appendix A.

	First campaign	Second campaign
Starting date	19/02/2018	14/09/2018
First profile	01/03/2018	14/09/2018
Ending date	13/04/2018	26/10/2018
IPM 1	Linear strips (Y)	Log strips (X)
IPM 2	Hamamatsu MCP (Y)	Photonis MCP (Y)
IPM 3	Log strips (Y)	Linear strips (Y)

Table 2.2: Summary of the two campaigns.

2.3 Image processing

At IPHI, cross section is higher than at ESS, so signal is easily recovered from a raw image. Therefore, no specific algorithm has been developed for filtering noise. A FFT filter can be use to remove patterns from camera sensor. Next prepossessing steps consist of removing hot pixels, correcting perspectives and/or orientation if necessary, selecting a region of interest. The beam profile is obtained by summing pixels in the region of interests. Figure 2.3 shows a example of a raw image and its resulting profile.

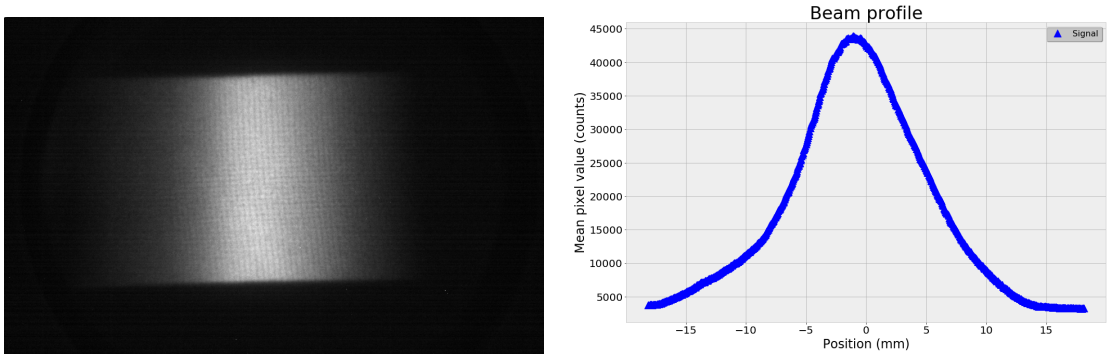

(a) Raw image from camera.

(b) Pixel summation along the longitudinal direction gives the beam profile.

Figure 2.3: Example of profile measurement with optical IPM.

2.4 Beam measurements

2.4.1 Position

As explained in the previous section, an important moment in our tests was when the BPM systems were restarted. The position given by the BPMs and the optical IPM can be plotted easily like in the Figure 2.4. For the first time, we were able to compare our measurement with an other device. Admittedly, this is not a profile comparison but we clearly saw the same beam instabilities which occur at IPHI. A variation exceeding 2 mm (5% of our readout size) can be observed from pulse to pulse. We dealt with it.

2.4.2 Current

IPHI has been designed to work at high current (above 50 mA), however our project requires lower intensities. At low current, the beam shape looks like a composition of two Gaussians, as shown Figure 2.5. We supposed that the tighter Gaussian is the beam

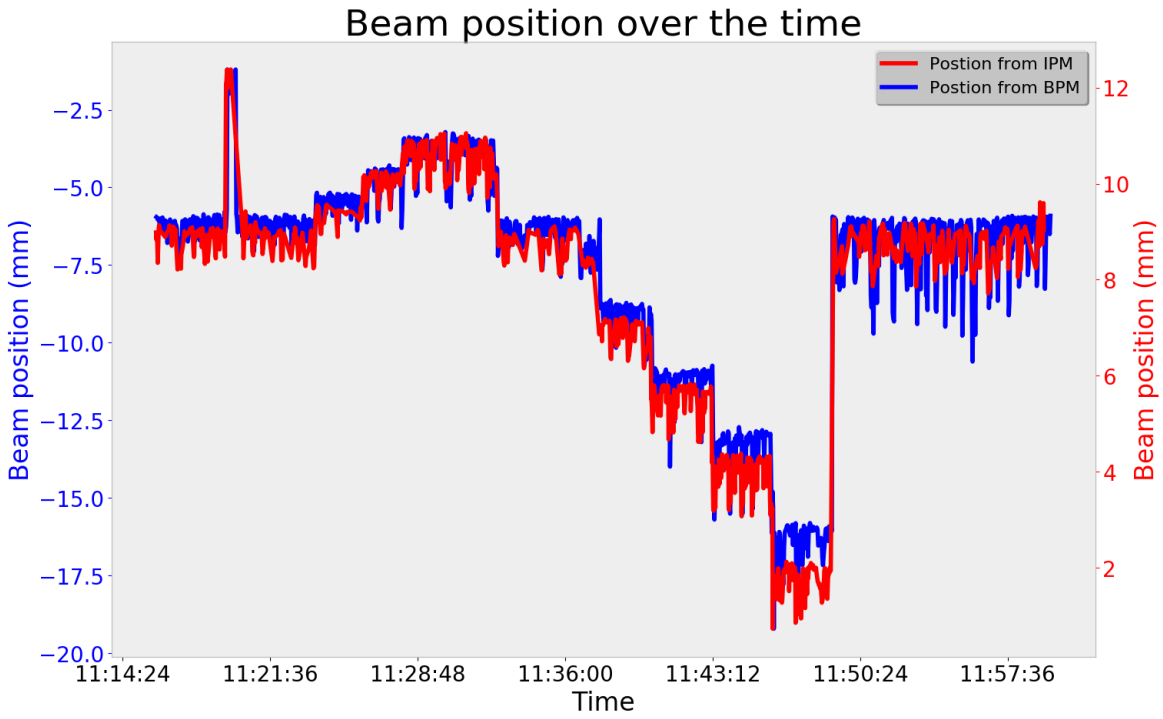

Figure 2.4: Beam position over the time measured with the BPM and the IPM. A steerer has been used to move the beam (step transitions). However, small variations between two steerer steps were not expected. Positions were directly extracted from IOCs without any processing.

core while the broader component is a kind of beam halo. At current higher than 50 mA, the beam core becomes bigger and completely overlaps the halo component. The beam core size increases linearly with the beam current. As a result, a single Gaussian fit may often fail and cannot be used properly to measure the beam size (Figure 2.5a). A simple statistical analysis of the profile distribution is also biased at low current or if the beam is not centered (Figure 2.5c). A workaround is to add a second Gaussian component into the fitting routine (Figure 2.5b). The measurement of the size can also be done by measuring the full width at the half magnitude. This method doesn't give directly the σ_{beam} but it is easy to implement, fast and stable (Figure 2.5d).

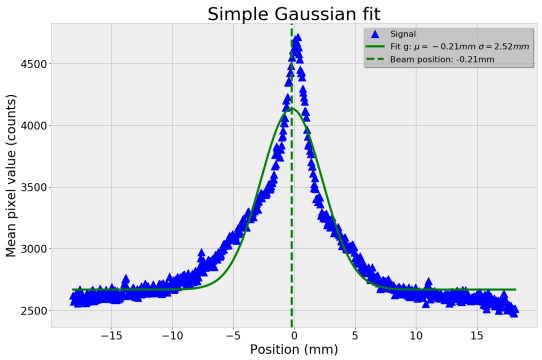

(a) Single Gaussian fit.

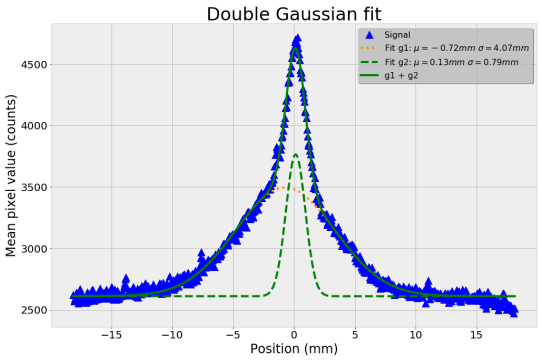

(b) Double Gaussian fit.

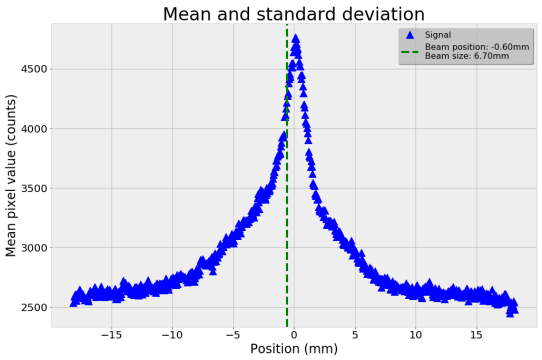

(c) Distribution measurement.

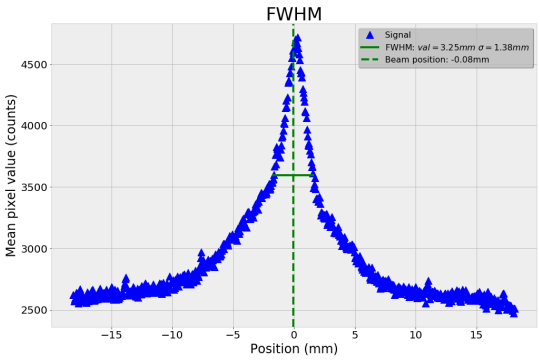

(d) Full Width at Half Magnitude.

Figure 2.5: Beam shape at very low current and different methods to measure beam size.

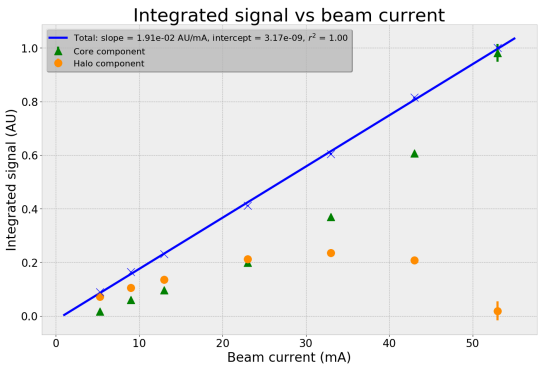

(a) Relative image intensity versus IPHI current.

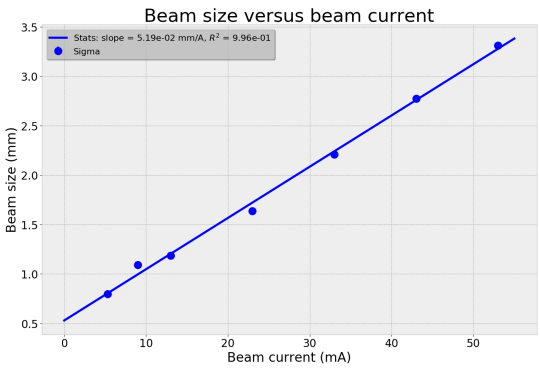

(b) Beam size versus IPHI current.

Figure 2.6: Influence of the beam current on beam shape.

2.5 Measurement on MCPs

2.5.1 Gain

Two different MPCs has been tested at IPHI, but not at same time since the Photonis MCP was not available[1] for the first campaign. The only difference we know is that the Photonis MCP has an open area ratio (OAR) of 60 while the Hamamatsu one has an OAR of 40. Hence, the amplification may be higher for the Photonis MCP. On the other hand, the Photonis one has a less sensitive phosphorus screen.

[1]We discovered a big crack on the MCP surface during the integration phase.

The following tests have been done on both MCP without significant change. The amplification of a MCP is related to the potential difference between its input and output. For a fixed beam current it is possible to plot the gain curve of the MCP. The gain follows an exponential behavior, as shown in Figure 2.7a. The influence of the MCP gain on the beam size has been also tested and seems to be negligible.

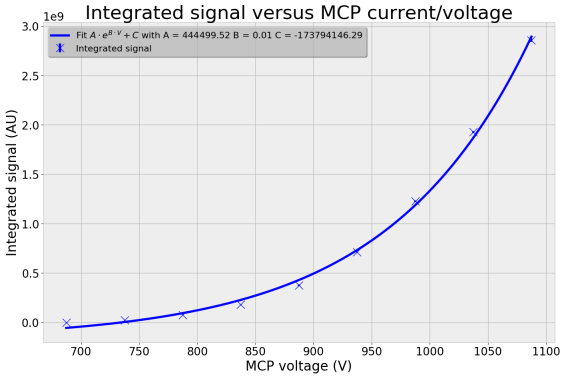

(a) Relative image intensity versus MCP voltage.

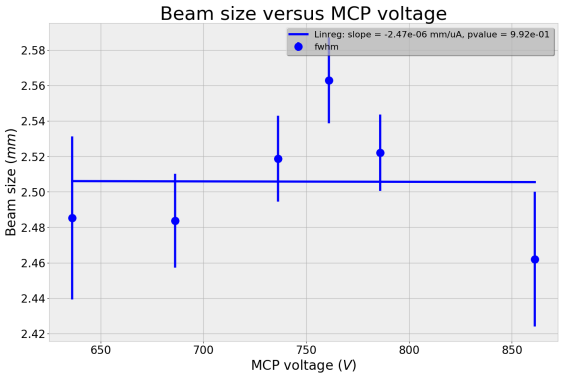

(b) Beam size versus MCP voltage.

Figure 2.7: Influence of MCP voltage on beam image.

2.5.2 Extrapolation to ESS condition

Unlike the strips IPM, it is almost impossible to quantify the number of primary particle. Hence, the extrapolation to ESS conditions is only done from Bethe Bloch formula, with respect to the beam parameters and vacuum conditions measured at IPHI. We supposed that the signal scale linearly with pressure[13]. The beam current and the pulse duration were set to their lowest values, respectively 0.7 mA and 50 μs. The pressure was about $4 \cdot 10^{-8}$ $mbar$ and its composition was mainly water (pessimistic hypothesis), see Appendix B. Table 2.3 sums up the factor of each parameter on the extrapolation.

ESS energy (MeV)	Bethe Bloch	Pressure	Gas composition	Intensity	Pulse length	Total
90	$\times 15$	$\times 40$	$\times 2.2$	$\div 89$	$\div 57$	$\times 0.26$
200	$\times 19$	$\times 40$	$\times 2.2$	$\div 89$	$\div 57$	$\times 0.33$
500	$\times 45$	$\times 40$	$\times 2.2$	$\div 89$	$\div 57$	$\times 0.78$
1000	$\times 56$	$\times 40$	$\times 2.2$	$\div 89$	$\div 57$	$\times 0.97$
2000	$\times 61$	$\times 40$	$\times 2.2$	$\div 89$	$\div 57$	$\times 1.06$

Table 2.3: Extrapolation from a real case during second campaign. The IPHI current was below 0.7 mA with a pulse duration of 50 μs. Pressure level was $4 \cdot 10^{-8}$ $mbar$ with mainly water vapors (pessimistic hypothesis). The scaling factor for each parameter is calculated from the nominal ESS beam conditions given in Table 2.1.

At first glance, it seems to be possible to measure single profile at nominal ESS conditions. However, this assumption is strongly dependent to the vacuum conditions. Neither the RGA nor the gauges were calibrated so the uncertainty may be relevant.

2.6 Phosphorus screens

2.6.1 Gain

A phosphorus screen converts a charged particle to visible photon. The signal amplitude depends on the energy deposition of the particle in the phosphorus layer. In our case, the phosphorus screen is placed just after the MCP output, as shown in Figure 1.2b. So the signal is proportional to the accelerating voltage between the MCP output and the phosphorus screen. Two screens have been tested during the beam tests: the P43 and the P46. Each screen has its intrinsic characteristics like the yield, the emission wavelength and the decay time.

Figure 2.8 shows that both screens have a linear response with the voltage. The beam size seems to be not affected by the screen gain, as shown in Figure 2.9. According to Hamamatsu, the lifetime of a phosphorus screen is negligible with respect to the MCP lifetime.

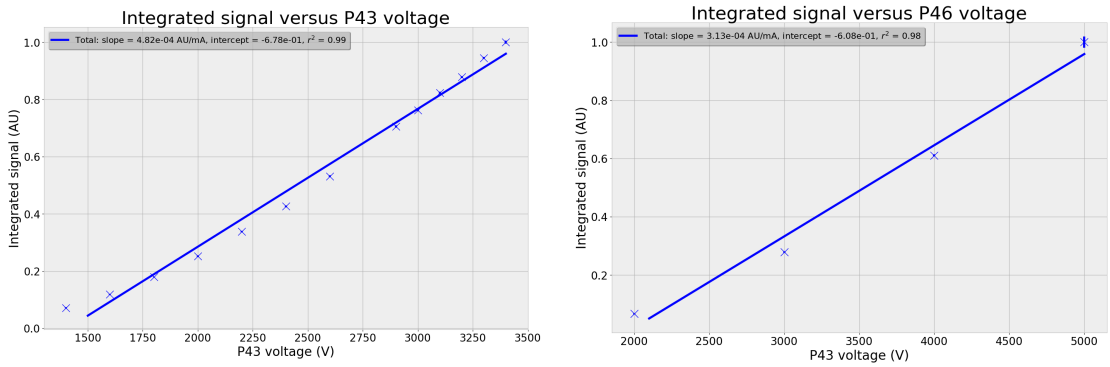

(a) P43 screen.

(b) P46 screen.

Figure 2.8: Relative image intensity versus phosphorus screen voltage.

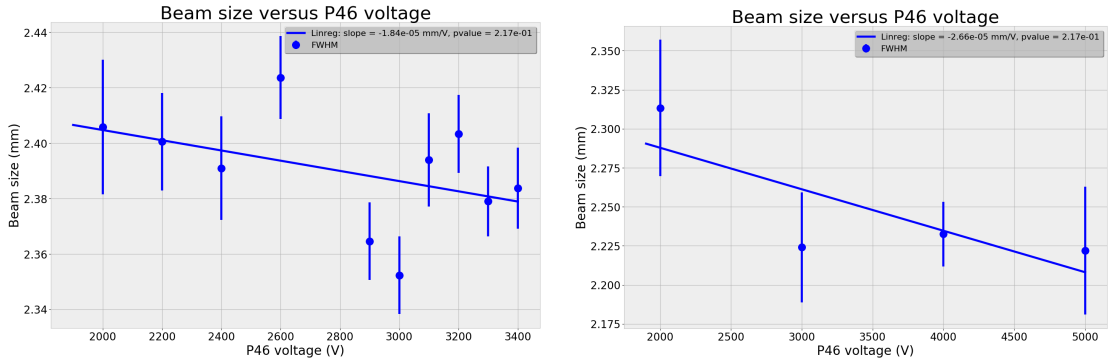

(a) P43 screen.

(b) P46 screen.

Figure 2.9: Beam size versus phosphorus screen voltage

2.6.2 Timing

The measurement of decay time has been performed by moving the camera trigger at small exposure times. The measurement is little more difficult for the fast screen. Indeed, the exposure time is now comparable to the decay time, also the delay and the jitter on the exposure time may afflict the measurement, see Appendix C.

As expected, the P43 is slow, thus if this screen is used for ESS then the total integration time on camera should be set to 10 ms and not strictly to 2.86 ms. This is not the case with the P46 screen.

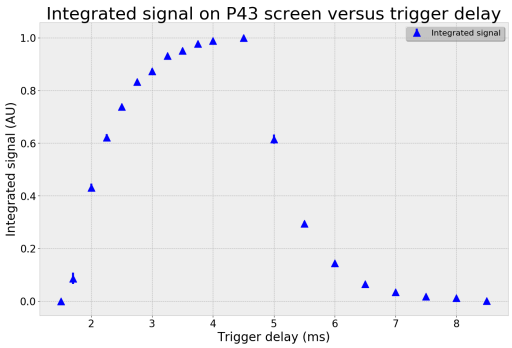

(a) P43: efficient but slow screen. At ESS, the pulse length will be far longer than IPHI.

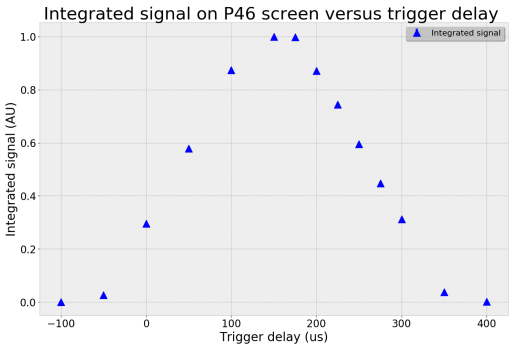

(b) P46: fast but less efficient screen. Conventional cameras are not supposed to work at such small exposure time, thus it gives only an approximation of its decay time.

Figure 2.10: Temporal responses for P43 and P46 screens. The pulse duration is around 100 μs.

2.7 High voltage studies

2.7.1 Extraction field

The extraction voltage is an important parameter of an IPM, if the electrical field is too low then profiles will be distorted by thermal motion and space charge effects. Those effects can be compensated by increasing the electrical field in the cage. At certain point the beam size will start to converge to its real value. This behavior has been observed with both strip and optical IPMs. Figure 2.11 shows the results from optical one.

However, reaching high voltage is a tricky business that may increase the complexity and reduce the stability of the detector. For example during the first campaign the optical IPM was not able to work at field higher than 70 V/mm and didn't work in symmetric configuration. Minor modifications had been done on prototype in order to reach 200 V/mm during the second campaign.

At IPHI, an electrical field of 100 V/mm was enough to observe the convergence. For ESS, it may be not the same due to space charge effect. The maximum operating voltage should be chosen according to the space charge simulations.

2.7.2 Symmetric and asymmetric fields

Simulations have been performed with COMSOL to cover both cases of asymmetric and symmetric configuration (see Appendix D for short summary). The simulations shows a good uniformity with a slightly better result for symmetric configuration. However, it may be difficult to quantify the uniformity at IPHI since the beam cannot be moved in a non uniform areas of the detector.

A possible workaround is to use the symmetric degraders in the asymmetric configuration. In this case the field is no more uniform and will affect the beam size and

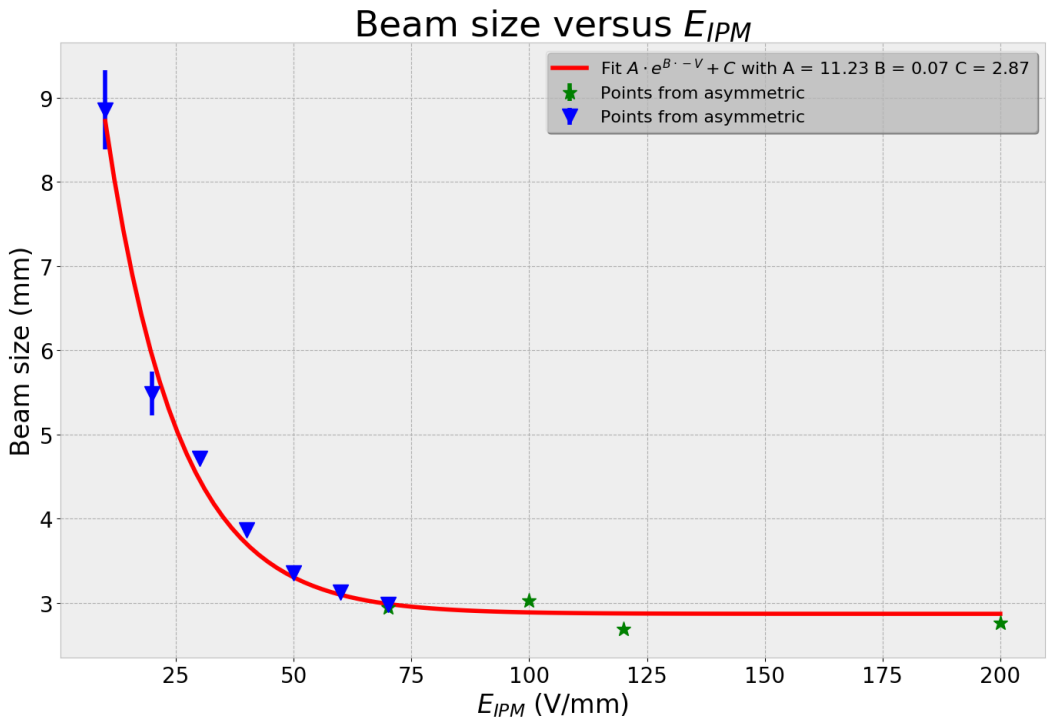

Figure 2.11: Beam size versus IPM electrical field. The beam size converge at $100V/mm^{-1}$

position. The field can be simulated in same way as previously by COMSOL. The three main effects have been observed from the simulations (see Figure D.4 in Appendix D). Firstly, the beam image is smaller than the real beam size. This focusing effect is constant over the overall plane detection. Secondly, the field tends to pull the beam image in the center of the detector. Thus, the measured displacement is less important on the image. Lastly, the beam image intensity is smaller in asymmetric because some particles are lost in the longitudinal direction. However, this effect can not be measured due to the difference of MCP gain between asymmetric and symmetric mode.

We measured the beam size and displacement for several steerer values in the symmetric and asymmetric configuration. The extractions field were set to same value for both configurations and all other parameters were frozen. If we suppose that the symmetric mode gives the real beam position and size, hence it is possible to quantify the difference between the simulations and experimental values. Results show good agreement between simulation and experimental values, as presented in Figure 2.12. It gives a certain confidence on the electrical field simulations.

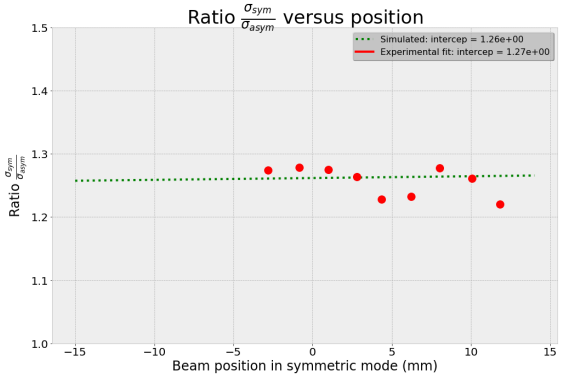

(a) Beam size ration between symmetric and asymmetric configurations at different relative beam position.

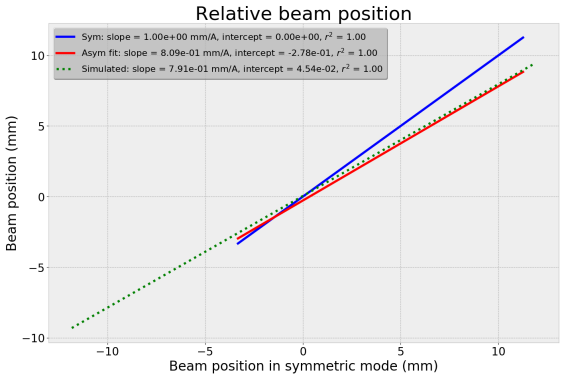

(b) Relative beam displacement in symmetric and asymmetric configurations.

Figure 2.12: Results of comparison between electrical field simulations and experimental data.

2.8 Electrons

Unfortunately, we were not able to measure any profile in electron mode during the first and second campaign. Typical pictures in electron configuration are shown in Figure 2.13. MCP may be a little less sensitive to electron compare to ions at same energies between five and ten keV [14]. However, during tests, without any modifications of the gain, the signal was always far higher for electrons. Hence, we suppose that the electron background is huge at IPHI. During tests, permanent magnets have been installed close to the aperture and beam dump. No clearly improvements have been observed. We still don't know exactly why there is so many electrons.

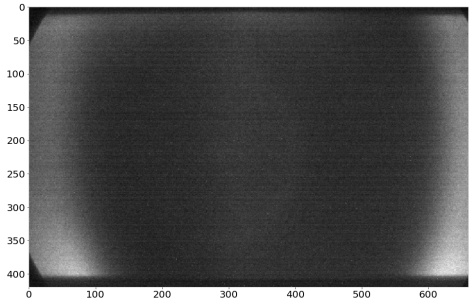

(a) Profile measurement attempt with electrons, Hamamatsu MCP

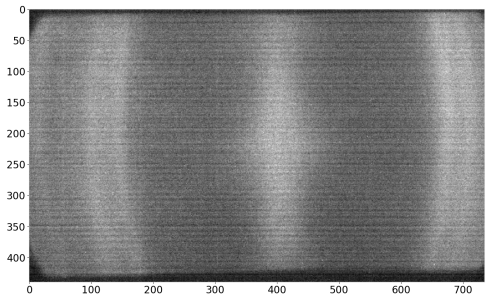

(b) Profile measurement attempt with electrons, Photonis MCP

Figure 2.13: Example of images in electron mode for both MCPs. Some patterns seem to be the same in the edges and middle of images. Line in the middle is not correlated with the beam.

2.9 Strips

2.9.1 Charge

When using one strip read-out with the FASTER DAQ (see §1.6), the information stored for such detector is:

- card number: 1 or 2, according to which $caramel$ daughterboard the strip detector is connected.
- channel number: from 1 to 32.
- charge (pC) collected in the strip corresponding to the channel number
- flag, for each channel, giving information about: missing data point (-1), saturated signal (1), not saturated signal (0)

It is possible to compare the charge collected by two strip detectors by simply integrating on all channels the signals detected in each strip after subtracting the electronic noise and the offset. In symbols:

$$Q = \sum_{n=1}^{(\#\ of\ \ strips)} q_i^{cleaned} = \sum_{n=1}^{(\#\ of\ \ strips)} (q_i^{detected} - q_i^{offset} - q_i^{electronic\ \ noise})$$

The sum of the electronic noise and offset will be always called from now on the "pedestal" or "pedestal level" [2], therefore:

$$Q = \sum_{n=1}^{(\#\ of\ \ strips)} (q_i^{detected} - q_i^{offset} - q_i^{electronic\ \ noise}) = \sum_{n=1}^{(\#\ of\ \ strips)} (q_i^{detected} - q_i^{pedestal})$$

Unfortunately the detectors have different dimensions. Moreover they are positioned at different locations, and they were used to measure two profiles in two different directions. Therefore it is practically impossible to compare the total charge per bunch collected in each read-out. Anyhow, what can be done, is measuring the ratio of the charges collected at two different beam intensities with the same read-out and comparing these ratios with what expected.

Strip read-outs "calibration"

The calibration of the two strips read-outs simply consisted in looking at the pedestal level and comparing it with what expected. The offset boxes, in the last part of the second campaign, were modified to provide the same baseline of 8.19 nA in each of the 32 output channels. If the integration time set on the DAQ is 100 μs, we expect therefore to collect, in every channel, a charge equal to:

$$Q_i^{offset} = \int_0^{10^{-4}\ s} (8.19 \cdot 10^{-9}\ A)\ dt = 8.19 \cdot 10^{-13}\ C = 0.819\ pC$$

The electronic noise is far smaller than this, therefore we can expect:

$$Q_i^{pedestal} \approx Q_i^{offset}$$

In Fig. 2.14 the measured pedestal level for each used channel is shown. For these plots only a minimal part of the available statistics has been used. The values of the pedestal levels of each channel connected to a physical strip for both read-outs and its error bar is reported in Tables 2.4 and 2.5.

[2] In reality the pedestal level is the electronic noise of the system when used in auto-triggered mode (i.e. when it does not trigger on external events). Anyhow, in this report we call pedestal level the baseline, i.e. electronic noise + offset level.

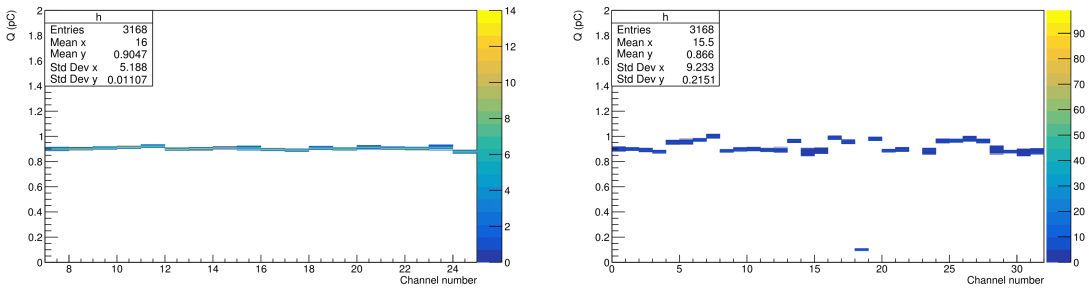

(a) Gaussian strips

(b) Linear strips

Figure 2.14: Measured pedestal level in the Gaussian (a) and Linear (b) read-outs. In (a) only 18 channels are used, in (b) channels 18 and 22 are not properly working.

Channel #	7	8	9	10	11	12	13	14	15
$\overline{pedestal}$	0.9015	0.9013	0.9089	0.9145	0.9238	0.8990	0.9032	0.9094	0.9096
$\sigma_{pedestal}$	0.0050	0.0044	0.0060	0.0049	0.0052	0.0048	0.0048	0.0054	0.0042
Channel #	16	17	18	19	20	21	22	23	24
$\overline{pedestal}$	0.9965	0.8921	0.9080	0.9007	0.9131	0.9061	0.9039	0.9138	0.8783
$\sigma_{pedestal}$	0.0047	0.0048	0.0052	0.0047	0.0053	0.0046	0.0049	0.0073	0.0053

Table 2.4: Pedestal value of each strip of the gaussian detector.

Charge measurements

A total of 4 measurements has been considered. In these measurements the two NPMs were exploited in the same conditions (same HV, same DAQ parameters) and in the same time. Only the beam intensity was changed from run to run, and as a consequence the pressure of the residual gas varied. The RGA spectrum corresponding to these measurements is reported in Fig. 2.15.

For comparison, also the camera data were included. No calibration was performed: the values reported for the cameras are calculated by projecting the image on the Y axis and integrating on 960 pixels. The pedestal was not calculated pixel by pixel, but simply by fitting the tails of the projections and assuming it is the same for each pixel. Table 2.6 reports the charge -or charge equivalent for the camera- measured for the different read-outs and is comprehensive also of the number of expected charges calculated from the Bethe-Bloch formula and the Garfield++ [15] code[3], while Table 2.7 puts in evidence the systematics of the results.

From Table 2.7 it can be inferred that the measured gas pressure has quite big uncertainty. The linear and gaussian read-outs seem to agree in relative value between each other, apart for the point at really low beam intensity. Since the routines used to analyze the data are the same, this is more a problem of the particular run than of the implemented algorithm. The camera data confirms the result of the gaussian strips.

Fig. 2.16 shows the linear trend of the camera data with respect to the beam intensity. The same trend is visible, for the same range, in the gaussian strips read-out, but is lost at higher beam intensities. Since no comparison with camera data is available at high beam intensities for this set of data, the lower detection limit of the gaussian strips for the present run conditions was extrapolated both by fitting the first 3 points and all points. In the first case a detection limit of 0.5 mA was obtained, while in the second 1.9 mA. The run conditions were:

[3]It is important to underline that the two calculations give the same value for the energy deposited in the gas but different number of electron/ion pairs created.

Channel #	0	1	2	3	4	5	6	7	8	9	10	11	12	13	14	15
$\overline{pedestal}$	0.8996	0.8985	0.8921	0.8786	0.9551	0.9548	0.9715	1.001	0.8830	0.8954	0.8970	0.8904	0.8886	0.9642	0.8758	0.8845
$\sigma_{pedestal}$	0.0063	0.0052	0.0055	0.0047	0.0067	0.0069	0.0064	0.0073	0.0048	0.0058	0.0055	0.0054	0.0079	0.0064	0.0112	0.0100
Channel #	16	17	18	19	20	21	22	23	24	25	26	27	28	29	30	31
$\overline{pedestal}$	0.9875	0.9538	0.9934	0.9789	0.8856	0.8927	0.000	0.8874	0.9638	0.9659	0.9805	0.9630	0.8947	0.8770	0.8770	0.8796
$\sigma_{pedestal}$	0.0071	0.0070	0.0033	0.066	0.0061	0.0056	0.0000	0.0082	0.0067	0.0061	0.0074	0.0064	0.0141	0.0053	0.0091	0.0080

Table 2.5: Pedestal value of each strip of the linear detector.

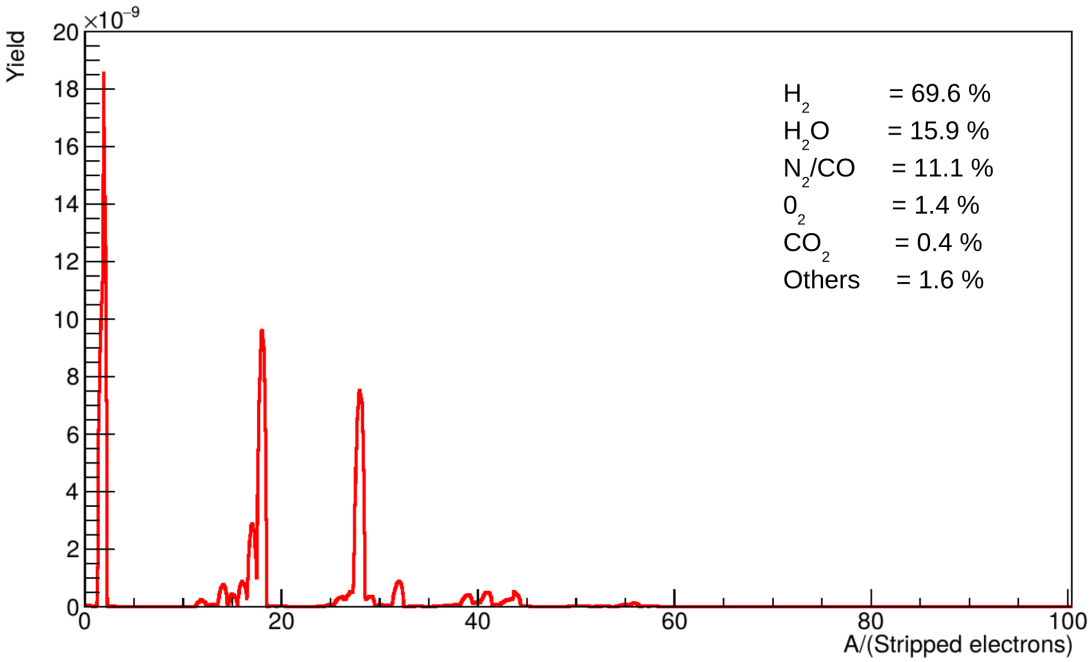

Figure 2.15: RGA spectrum. The other gases should be CH_4 (0.6%), C_2H_6 (0.4%) C_3H_8 (0.1%) C_3H_6 (0.3%) and unknown masses (0.2%)

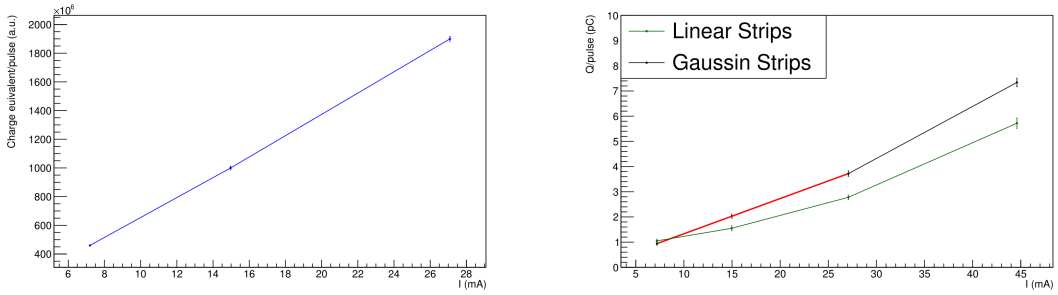

(a) Camera (b) Strips

Figure 2.16: Linearity of the signal collected on different read-outs as a function of the beam intensity.

- $\Delta t_{pulse} = 200\ \mu s$
- $t_{integration} = 100\ \mu s$

RUN	I (mA)	p (mbar)	GAUSSIAN STRIPS Q $\pm\sigma_q$ (pC/pulse)	LINEAR STRIPS Q $\pm\sigma_q$ (pC/pulse)	CAMERA Q $\pm\sigma_q$ (arb. unit)	EXPECTED B-B Q (pC/pulse)	EXPECTED G++ Q (pC/pulse)
1	7.2	2.90 10^{-8}	0.94 $\pm$ 0.06	1.05 $\pm$ 0.07	4.6 10^{8} $\pm$ 6.4 10^{6}	0.119	0.119 *0.52
2	14.97	7.50 10^{-8}	2.03 $\pm$ 0.08	1.55 $\pm$ 0.10	1.0 10^{9} $\pm$ 1.3 10^{7}	0.649	0.649*0.52
3	27.09	6.60 10^{-8}	3.72 $\pm$ 0.11	2.78 $\pm$ 0.09	1.9 10^{9} $\pm$ 1.7 10^{7}	1.034	1.034 *0.52
4	44.6	1.10 10^{-7}	7.34 $\pm$ 0.17	5.72 $\pm$ 0.21	different gain	2.735	2.735*0.52

Table 2.6: Charge collected on different read-outs as a function of the beam intensity.

RUN	GAUSSIAN/GAUSSIAN	LINEAR/LINEAR	CAMERA/CAMERA	EXPECTED/EXPECTED	INTENSITY/INTENSITY
1/2	0.47 $\pm$ 0.02	0.68 $\pm$ 0.04	0.45 $\pm$ 0.01	0.18	0.48
2/3	0.55 $\pm$ 0.02	0.55 $\pm$ 0.02	0.54 $\pm$ 0.01	0.62	0.55
3/4	0.51 $\pm$ 0.01	0.49 $\pm$ 0.02	different gain	0.38	0.60

Table 2.7: Ratios of the charge collected on a same read-out at two different beam intensities.

- HV = 20 kV
- E_p = 3 MeV
- p = 1.1 10^{-7} mbar (worst pressure value)

According to calculations performed using the Bethe-Bloch formula, at ESS in the Spoke section around 10^5 electrons/ion pairs will be created. The results given by Garfield++ is half of it. Fewer charges are expected at higher proton energies, in the medium-β and high-β sections of the accelerator. An IPHI beam of 0.5 mA corresponds to about 10^5 electron/ion pairs produced. This, which is the most optimistic lower limit achieved during the second measurement campaign, rules out the possibility of using the strip read-out at ESS. The lowest detection limit obtained in this measurement campaign is almost 10 times larger (10^6 electron/ion pairs).

Chapter 3

Space Charge

The effects of space charge are twofold: they affect the charged particle beam itself and any other charge in its proximity. Our focus is on this second aspect. A charge generated at rest between two parallel plates kept at different voltages drifts towards the electrodes travelling parallel to the electric field lines. In an ideal case of perfectly uniform electric field, the point where the charge meets the plate will simply be the projection of its initial position on the electrode. In IPMs, charges are created via gas ionization and the beam profile is reconstructed this way. But the presence of a charged particle beam, necessary to create ionization charges, induces an electromagnetic field which modifies the trajectories of the electrons and of the ionized gas molecules and thus introduces a shift between the point where they should have ideally meet the electrode and the point where they really reach it. The measured beam profile therefore will differ from the real one by an amount which depends on the beam intensity, the beam size, the beam energy and the strength of the electric field applied between the electrodes.

An in-house algorithm to estimate the influence of space charge at ESS have been implemented at Lund and completed at Saclay to account for realistic electric fields and initial momenta of the ionization charges. Its mathematics is based on [16].

3.1 Results guide-lines

3.1.1 Convention

In the next pages, the following convention is used:

- σ_{x_i}, σ_{y_i} and σ_{z_i} : initial beam width along x, y and z used as input in the simulations assuming the beam has a 3D Gaussian shape.
- σ_x, σ_y and σ_z : final beam width along x, y and z obtained from the simulations.
- $\vec{E} = \mathrm{E}_y$ means that $\vec{E} \,/\!/\, \vec{y}$ and therefore the components along the axis $\perp \vec{y}$ are null (i.e. $\mathrm{E}_x = \mathrm{E}_z = 0$).
- the proton beam is moving along the positive direction of the z axis
- the space charge effect is quantified as Δ_x (%), which is the deviation between the beam width input in the simulations and the one obtained by running the code.

3.1.2 Simulations outcomes

The space charge effects have been initially calculated for different beam energies (90 MeV, 200 MeV and 1 GeV), beam widths (σ_{x_i} = 1.2 mm, 1.6 mm, 2 mm, 2.4 mm and 2.8 mm, σ_{y_i} = 1.2 mm, 1.6 mm, 2 mm, 2.4 mm and 2.8 mm and σ_{z_i} = 2 mm) and uniform electric fields (from 50 kV/m to 300 kV/m) both for electrons and for the H_2^+ ions. The choice of simulating the space charge effects felt by ionized molecules of hydrogen originates from the fact that the H_2 is expected to account for 79 % in volume of the nominal residual gas composition in the beam line.

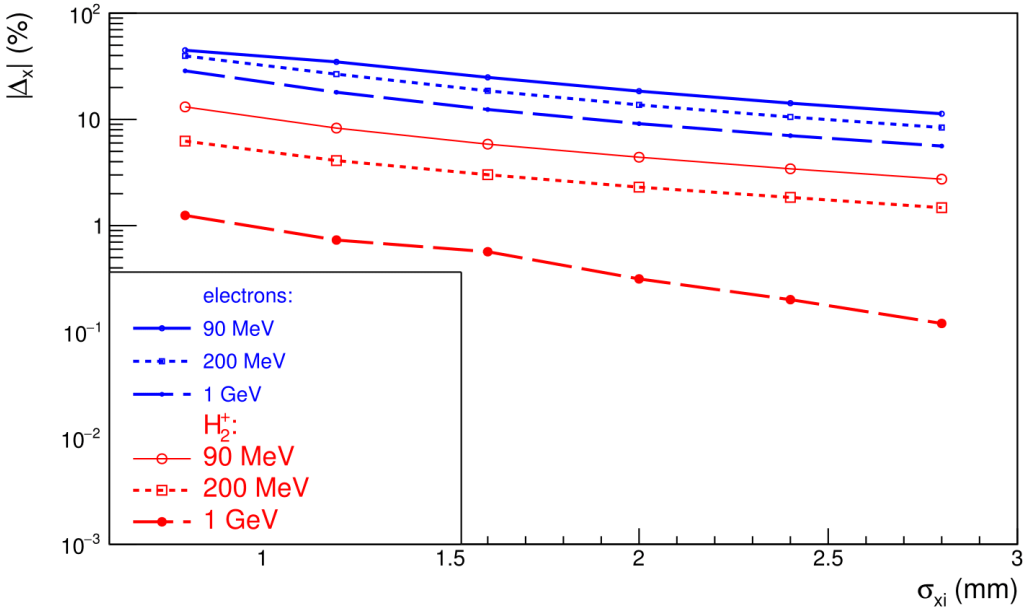

Figure 3.1: Space charge effects for different σ_{x_i} and incident beam energies when $\sigma_{y_i} = \sigma_{z_i}$ = 2mm and $\vec{E}$ = E_y = 300 kV/m.

Fig. 3.1 reports the trend of the space charge effects with respect to different σ_{x_i}, beam energies and test particles when $\vec{E}$ = Ey = 300 kV/m, and both the σ_{y_i} and σ_{z_i} input in the simulation measure 2 mm. It is evident that the lower the beam energy and the higher is the deviation between the input beam width and the one obtained by running the code. This is true for the particular simulations run, but it is not a general rule. As a matter of fact, for a different set of electric field strength and σ_{x_i}, σ_{y_i} and σ_{z_i} values, the opposite behaviour can be obtained. This underlines the complexity of the phenomenon, which results from the interplay of various factors. Nevertheless, it is possible to draw some conclusions. First, the larger the initial beam width and the lower the space charge effects. Finally, the discrepancy between the beam width input in the simulations and the one obtained as their results is larger for electrons than for ions, due to their high difference in mass.

In Fig. 3.2 the trend of the space charge effects as a function of a homogeneous electric field $\vec{E}$ = E_y is studied only for lowest possible energy of the cold Linac cryomodule (90 MeV), i.e. for the worst case scenario of the results of 3.1. The values of σ_{x_i}, σ_{y_i} and σ_{z_i} were fixed to 2 mm, which corresponds to the average beam size in the Spoke section of the accelerator. As expected, the lower the field, the lower the speed of the drifting test charges, the more time they spend in the electromagnetic field generated by the ESS beam and the larger the space charge effects. From Fig. 3.2 it can be inferred that if electrons are used to measure the beam profile, an electric field

higher than 10^6 kV/m is needed to meet the ESS uncertainty requirement of 10%. On the other hand, the same condition is fulfilled for much weaker electric fields if singly ionized hydrogen molecules are detected. A difference of potential of 15 kV between the two electrodes of the IPM cube of 10 cm side is already enough to measure the transverse profile with a maximum total error in the RMS extension of the beam of less than $\pm$ 10%.

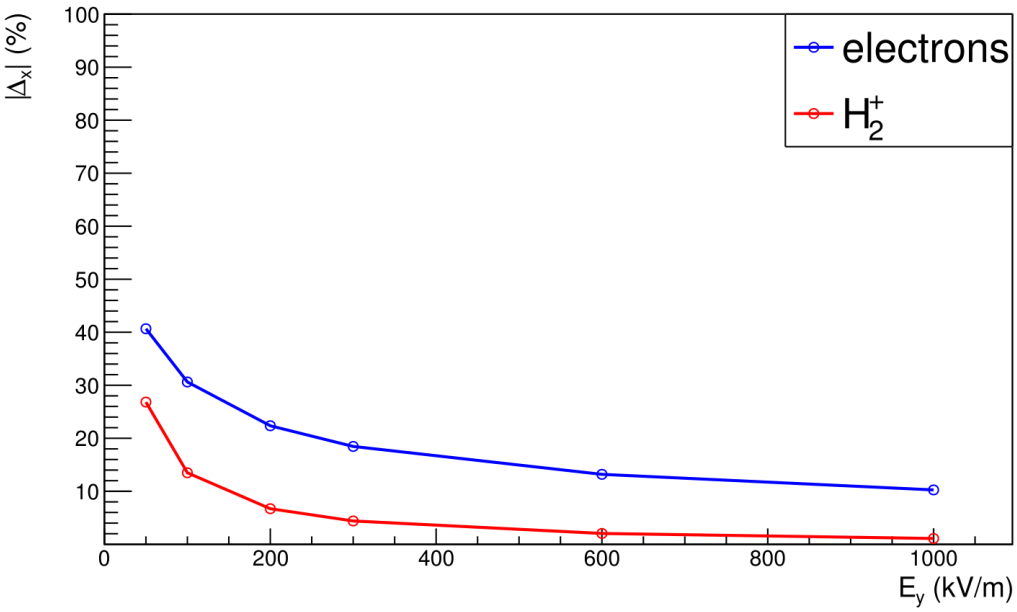

Figure 3.2: Comparison between the space charge effects for electrons and singly ionized hydrogen molecules H_2^+, for a 90 MeV proton beam with beam size $\sigma_{x_i} = \sigma_{y_i} = \sigma_{z_i} =$ 2 mm in an homogeneous electric field.

Since these simulations do not account for effects such as the space resolution of the detector, and are themselves affected by an uncertainty estimated to less than 2%, it was decided that an electric field higher than 150 kV/m is preferable. As a matter of fact, to more efficiently counterbalance the space charge effects, the electric field needs to be as high as possible. E_y = 300 kV/m has been selected as maximum electric field realistically reachable in the experimental set-up.

The results reported in 3.2 are obtained considering that electrons and ions are created at rest. This is not true and the impact of the initial momentum distributions of electrons and H_2^+ on the beam profile measurements has therefore been simulated. The outcome was that this factor is negligible for massive particles, but not for electrons. Fig. 3.3 shows the comparison between the results of the simulations run for the two test charges when the Spoke configuration (90 MeV proton beam with beam size σ_{x_i} $= \sigma_{y_i} = \sigma_{z_i} =$ 2 mm) and an homogeneous $\vec{E} = E_y =$ 300 kV/m are considered. For these conditions, if electrons are produced at rest, $\mid \Delta_x \mid < 25\%$, while it increases to $\mid 3.764 - 2 \mid 2 \sim 88\%$ when their initial momenta distributions are accounted for. For singly ionized hydrogen molecules instead $\mid \Delta_x \mid$ remains stable to $\sim 4\%$ both when they are generated at rest and with an initial momentum distribution. It is therefore evident that, to fulfill the ESS requirement, the IPMs can not be polarized in such a way to detect electrons on the read-out.

Finally, real case electric field simulations of two IPMs, orthogonal to each others were performed at CEA-Saclay and fed to the code. This allowed to check the influence of the other field components (E_x and E_z) on the transverse beam profile measurements.

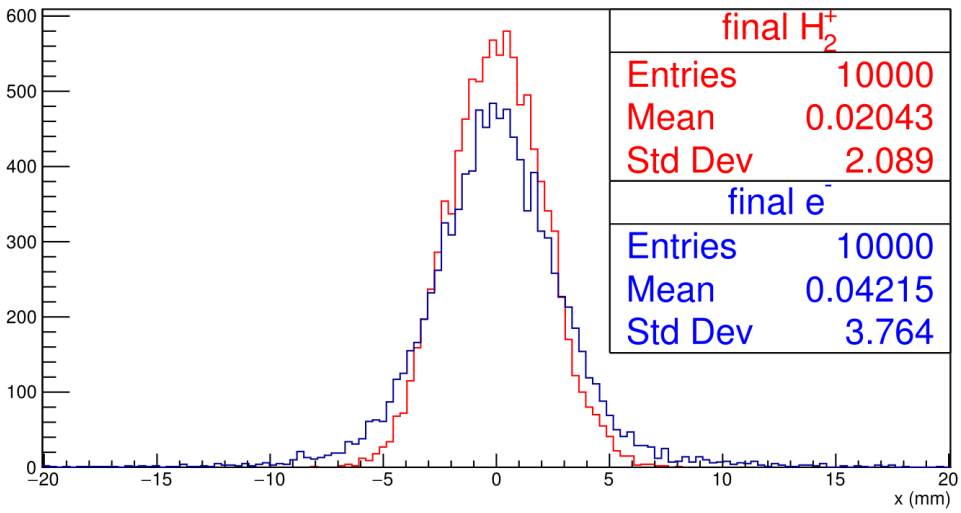

Figure 3.3: Comparison between the space charge effects felt by electrons and ions when initial momenta distributions are accounted for. Both test charges are created by a 90 MeV proton beam in the Spoke configuration and a perfectly homogeneous electric field $\vec{E} = E_y = 300$ kV/m has been considered.

Having proved that we can use IPMs only in ion configuration and that, in such a case, the initial momenta distributions can be neglected, a study for H_2^+ molecules created at rest was performed for Spoke conditions and three sets of resistors on the IPMs, giving rise to three different E_y^{COMSOL} field configurations aiming to be as close as possible to $E_y \rightarrow 75$ kV/m, $E_y \rightarrow 150$ kV/m and $E_y \rightarrow 300$ kV/m. Since resistors do not come with every desirable value, a choice towards sets resulting in a slightly focusing electric field was performed at the expenses of sets creating slightly unfocusing electric fields. This helps to counterbalance the impact of the space charge effects on the transverse beam profile measurements (see Fig. 3.4).

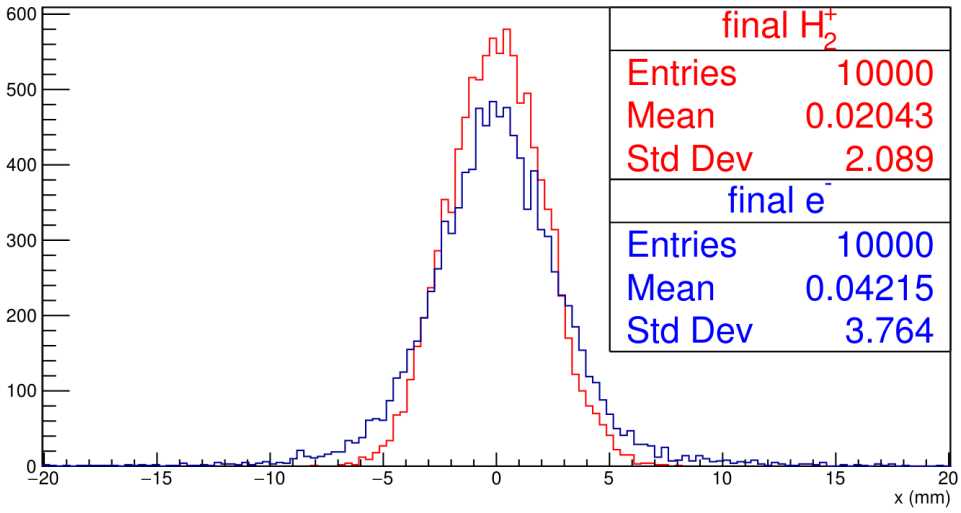

Figure 3.4: Space charge effects for singly ionized hydrogen molecules H_2^+ created at rest at Spoke conditions for different real case electric fields.

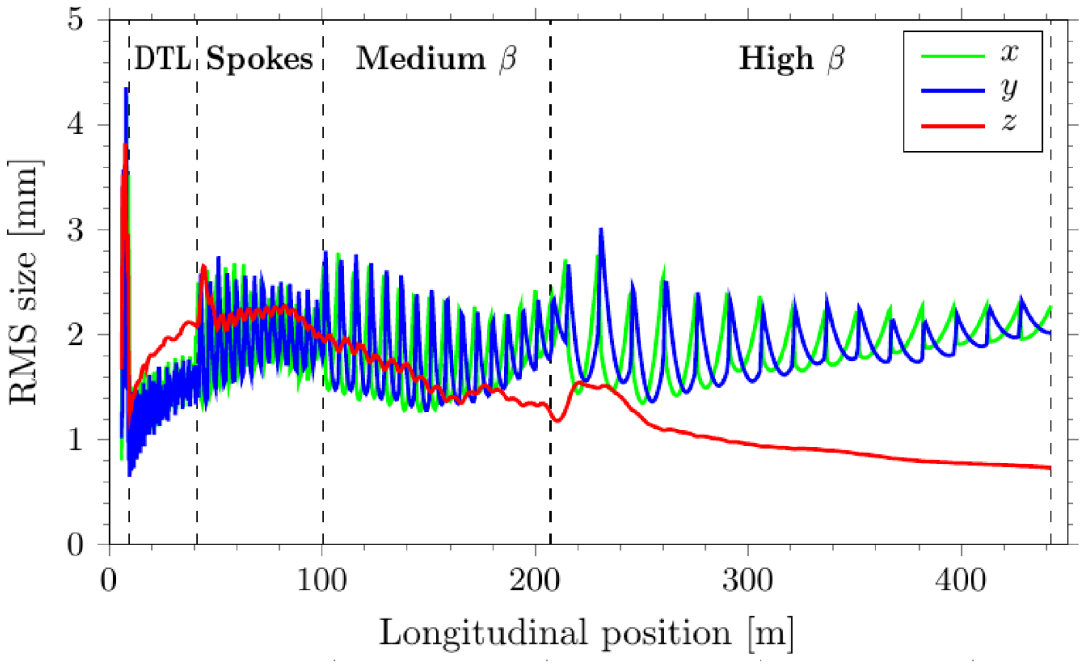

Figure 3.5: Expected beam width at ESS.

3.2 Final ESS simulation results

The following tables summarize the expected deviation of the measured beam width from the real one at ESS due to space charge effects. The σ_{x_i}, σ_{y_i} and σ_{z_i} are taken from Fig 3.5. They are the smallest beam width for the desired proton energy, therefore the worst case scenario.

For every simulation, the momenta of the ions at creation are considered. Since Garfield++ can provide this information only for electrons, a simplifying assumption was made. The problem was split in two parts: first the determination of the ion speed, and then their emission angle. For deriving the speed of the ions, it was assumed that the protons in the beam do not change direction after ionizing the gas. Therefore the initial "system" is composed by a proton moving along $\vec{z}$ with a certain momentum and a molecule at rest. Given the fact that most electrons are emitted at $\frac{\pi}{2}$, the final system is composed by the same proton, moving again along $\vec{z}$ practically with the same energy and by an electron and ionized molecule moving in opposite directions. In other words:

$$P_{\parallel}^{initial} = p_{\parallel}^{proton}$$

$$P_{\parallel}^{final} = p_{\parallel}^{proton}$$

$$P_{\perp}^{initial} = 0$$

$$P_{\perp}^{final} = p^{electron} + p^{ion}$$

with P momentum of the system and p momenta of the particles in the system.

Therefore:

$$v_{ion} = v_{electron}\frac{m_{electron}m_{ion}}$$

The angle at which the ions are emitted is chosen to be the same at which electrons were emitted according to Garfield++.

The electric field considered in the simulations was calculated with COMSOL, by carefully implementing the geometry of the IPMs in the LWU tube. The values of the resistors is not ideal, but chosen among the commercially available ones. In the COMSOL simulations one electrode was at ground, while the other was connected to HV (asymmetric field configuration). The IPM number one is the one closest to the beam entrance and will be used to measure the profile along the Y direction.

3.2.1 IPM1: Y profile

Test particle	**E_p MeV**	**E kV/m**	σ_{x_0} **mm**	σ_{y_0} **mm**	σ_{z_0} **mm**	σ_x **mm**	$\frac{\sigma_x-\sigma_{x_0}}{\sigma_{x_0}}$ **%**
H_2^+	90.0	200	1.25	1.25	2.80	1.285	2.783
H_2^+	90.0	250	1.25	1.25	2.80	1.273	1.879
H_2^+	90.0	300	1.25	1.25	2.80	1.267	1.355
H_2^+	153.0	200	1.60	1.60	2.20	1.608	0.477
H_2^+	153.0	250	1.60	1.60	2.20	1.602	0.144
H_2^+	153.0	300	1.60	1.60	2.20	1.599	-0.084
H_2^+	216.0	200	1.50	1.50	2.00	1.502	0.149
H_2^+	216.0	250	1.50	1.50	2.00	1.498	-0.101
H_2^+	216.0	300	1.50	1.50	2.00	1.496	-0.256
H_2^+	388.0	200	1.25	1.25	1.40	1.249	-0.048
H_2^+	388.0	250	1.25	1.25	1.40	1.247	-0.225
H_2^+	388.0	300	1.25	1.25	1.40	1.246	-0.344
H_2^+	516.0	200	1.80	1.80	1.20	1.789	-0.634
H_2^+	516.0	250	1.80	1.80	1.20	1.787	-0.705
H_2^+	516.0	300	1.80	1.80	1.20	1.786	-0.757
H_2^+	1280.0	200	1.60	1.60	0.90	1.588	-0.730
H_2^+	1280.0	250	1.60	1.60	0.90	1.587	-0.785
H_2^+	1280.0	300	1.60	1.60	0.90	1.587	-0.828
H_2^+	2000.0	200	2.00	2.00	0.70	1.983	-0.857
H_2^+	2000.0	250	2.00	2.00	0.70	1.982	-0.895
H_2^+	2000.0	300	2.00	2.00	0.70	1.982	-0.923

3.3 IPM2: X profile

Test particle	E_p MeV	E kV/m	σ_{x_0} mm	σ_{y_0} mm	σ_{z_0} mm	σ_x mm	$\frac{\sigma_x - \sigma_{x_0}}{\sigma_{x_0}}$ %
H_2^+	90.0	200	1.25	1.25	2.80	1.277	2.174
H_2^+	90.0	250	1.25	1.25	2.80	1.269	1.489
H_2^+	90.0	300	1.25	1.25	2.80	1.263	1.025
H_2^+	153.0	200	1.60	1.60	2.20	1.605	0.310
H_2^+	153.0	250	1.60	1.60	2.20	1.600	0.025
H_2^+	153.0	300	1.60	1.60	2.20	1.597	-0.159
H_2^+	216.0	200	1.50	1.50	2.00	1.501	0.056
H_2^+	216.0	250	1.50	1.50	2.00	1.498	-0.159
H_2^+	216.0	300	1.50	1.50	2.00	1.495	-0.311
H_2^+	388.0	200	1.25	1.25	1.40	1.249	-0.049
H_2^+	388.0	250	1.25	1.25	1.40	1.247	-0.243
H_2^+	388.0	300	1.25	1.25	1.40	1.246	-0.346
H_2^+	516.0	200	1.80	1.80	1.20	1.788	-0.666
H_2^+	516.0	250	1.80	1.80	1.20	1.787	-0.738
H_2^+	516.0	300	1.80	1.80	1.20	1.786	-0.781
H_2^+	1280.0	200	1.60	1.60	0.90	1.590	-0.644
H_2^+	1280.0	250	1.60	1.60	0.90	1.588	-0.720
H_2^+	1280.0	300	1.60	1.60	0.90	1.588	-0.758
H_2^+	2000.0	200	2.00	2.00	0.70	1.982	-0.913
H_2^+	2000.0	250	2.00	2.00	0.70	1.982	-0.924
H_2^+	2000.0	300	2.00	2.00	0.70	1.981	-0.947

3.4 IPHI measurements and simulations

In the first measurement campaign at IPHI the beam profile was measured with all read-outs along the same direction, giving a good agreement as shown in Fig. 3.6. For a fixed beam intensity, the trend of the beam width as a function of the H.V. was measured with the gaussian strips alone (no mcp). This trend is shown in Fig. 3.7. On the same

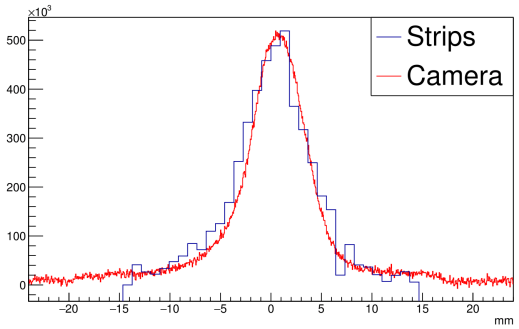

Figure 3.6: Beam profile measured with Linear strips and camera in the first campaign. Both set-up were equipped with an MCP.

plot the values of the beam width along the two orthogonal direction appear. The σ_z was estimated by running TraceWin simulations. In the geometry, a parallel beam was asked for, reproducing the IPHI beam in the experimental setup. In any case, whatever the assumptions, a large σ_z was obtained. Once two beam dimensions are fixed, by trial and error it was possible to estimate σ_y with the aid of the space charge algorithm.

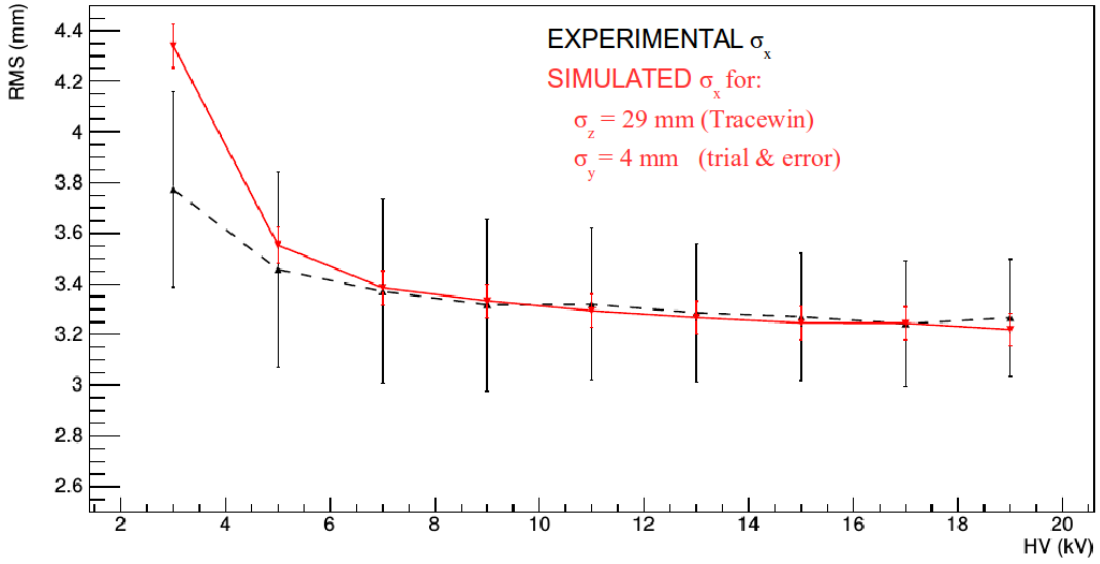

Figure 3.7: Trend of the beam width as a function of the HV measured for a fixed beam intensity with the gaussian read-out. An extrapolation of the beam width in the orthogonal direction was tempted with the aid of TraceWin and the in-house space charge effect algorithm.

In the second campaign it was decided to measure the beam profile in two orthogonal directions to validate the simulations. Unfortunately during this second set of measurements, the experimental conditions were not the same. As a result, both strip read-outs were dominated by background electrons and it was therefore not possible to determine with enough accuracy the beam width with these detectors.

Conclusions

Two kind of IPM prototypes has been tested at IPHI, a 3 MeV proton accelerator. Both of them were able to measure beam profiles at IPHI. The First conclusion from the tests shows that the use of an MCP is mandatory to detect signal at ESS conditions. Hence, optical IPM is the preferred solution since it provides higher sensitivity.

A relative check of the electrical field uniformity has been performed on both asymmetric and symmetric configurations and with an optical IPM. The results from the tests show a good agreement with COMSOL simulations. The choice of the HV symmetry will depend on power supply technology. With our current power supplies, we recommend the asymmetric configuration. On the other hand, more advanced power supplies are available from ISEG, and may allow the symmetric configuration to be implemented.

We validate our detectors and simulation models as much as experimental condition permitted. The advantages provided by the use of the IPHI accelerator were undermined as these tests were performed ahead of the accelerator commissioning. However, in spite of the instability of the machine and not so well-known beam conditions, a rather complete characterization of the prototypes has been achieved. From the lessons learned with the prototype, a final design of the cNPM is delivered, including few modifications from the prototype.

Some issues remain to be investigated, in particular MCP aging calibration, ESS background estimation and radiations effects on readout. Document ESS-0680910 covers more in detail these issues and gives outlooks for the final detector.

Appendices

Appendix A

More on beam tests

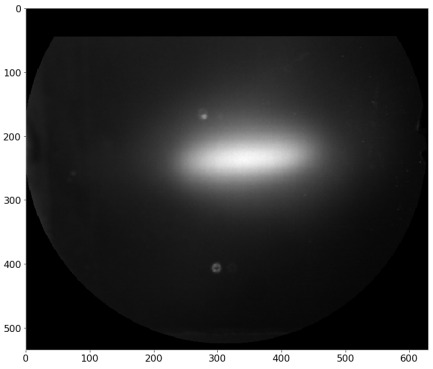

(a) First test campaign, the beam profile dispersion due to the dipole is clearly seen.

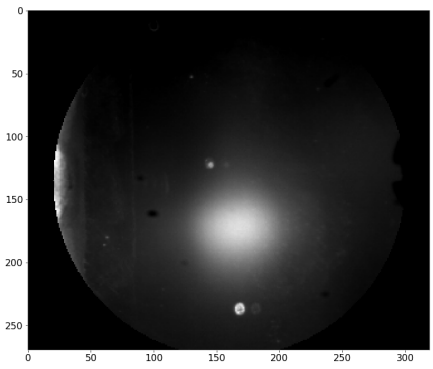

(b) Second test campaign, the beam profile in the dispersive plane was cut by the small collimator aperture.

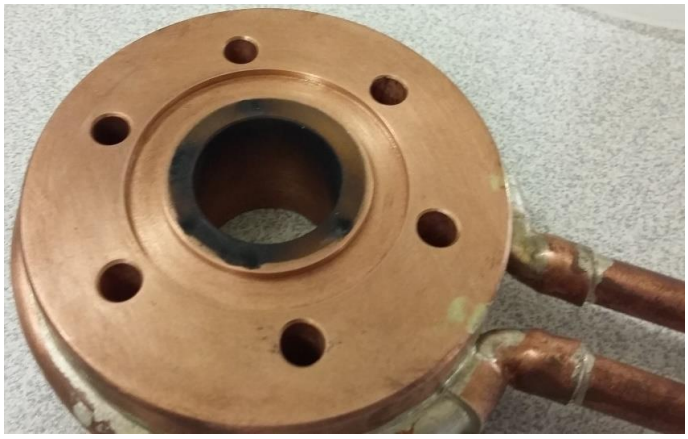

(c) A small water-cooled collimator aperture has been installed during the second campaign.

Figure A.1: Comparison of the beam shapes on scintillating screen between the two campaigns. As expected the small water-collimator aperture (Φ=25 mm) cuts the dispersive tail in the Y plane.

Appendix B

RGA Spectrum

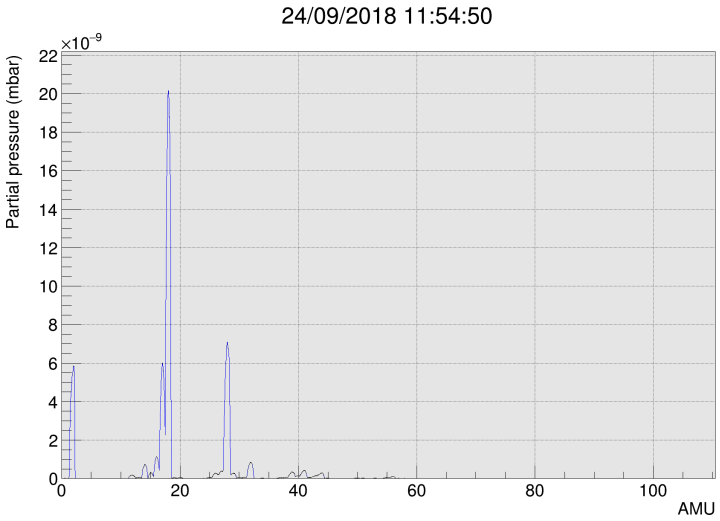

(a) RGA spectrum at the beginning of the beam tests. This spectrum is mainly dominated by water.

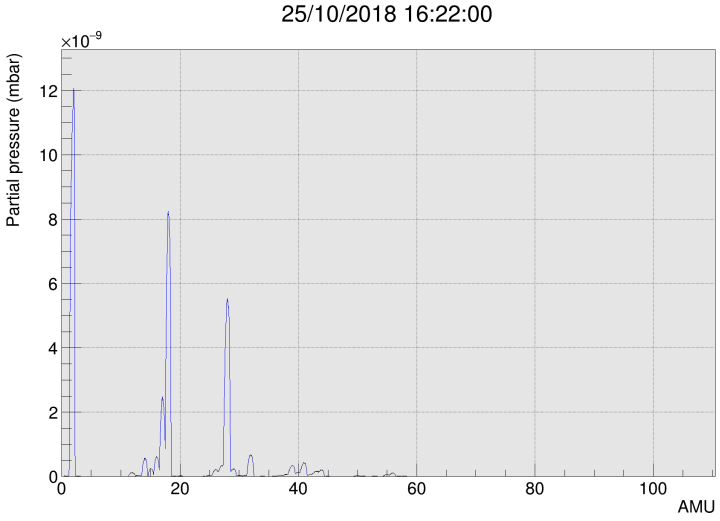

(b) RGA spectrum after few weeks of pumping. Now, hydrogen is predominant in the residual gas.

Figure B.1: Examples of RGA spectrum

Appendix C

Camera trigger

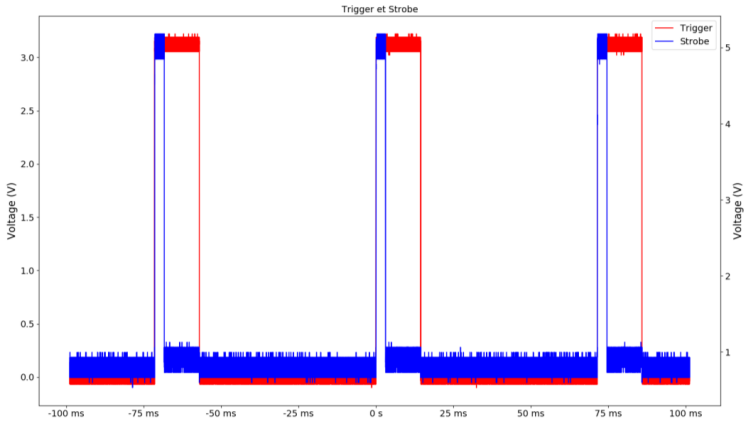

(a) Trigger repetition rate. The camera is able to work at 14 Hz.

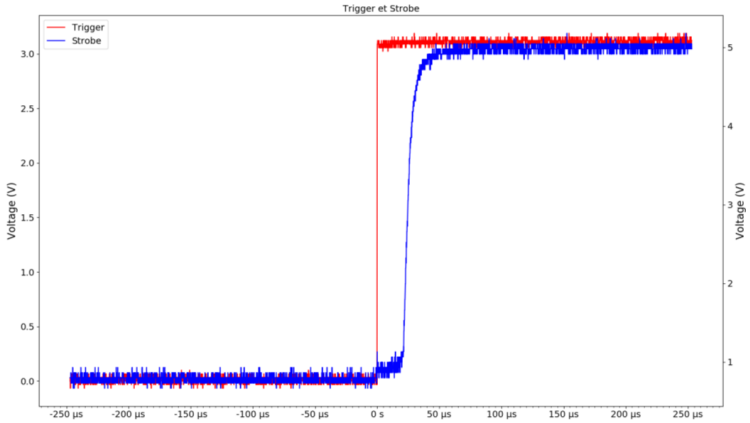

(b) Trigger delay. The delay on trigger is around 25 μs for the Blackfly camera. Measurement has been done with a 30 meters cable.

Figure C.1: Trigger signal (red) and camera feedback (blue).

Appendix D

Electrical field uniformity

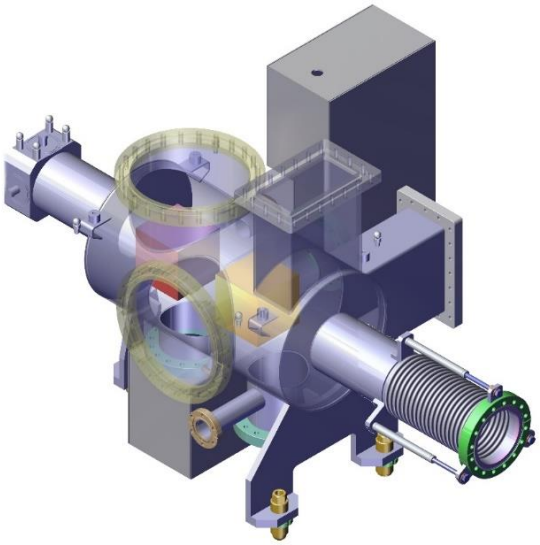

(a) LWU drawing.

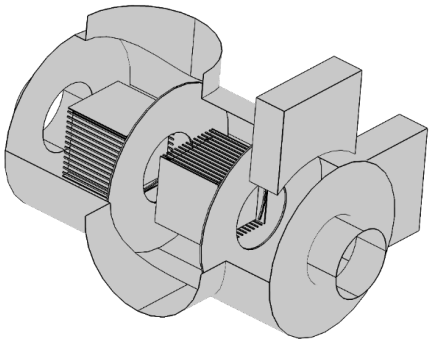

(b) COMSOL implementation.

Figure D.1: Simulation of electrical field has been done with COMSOL.

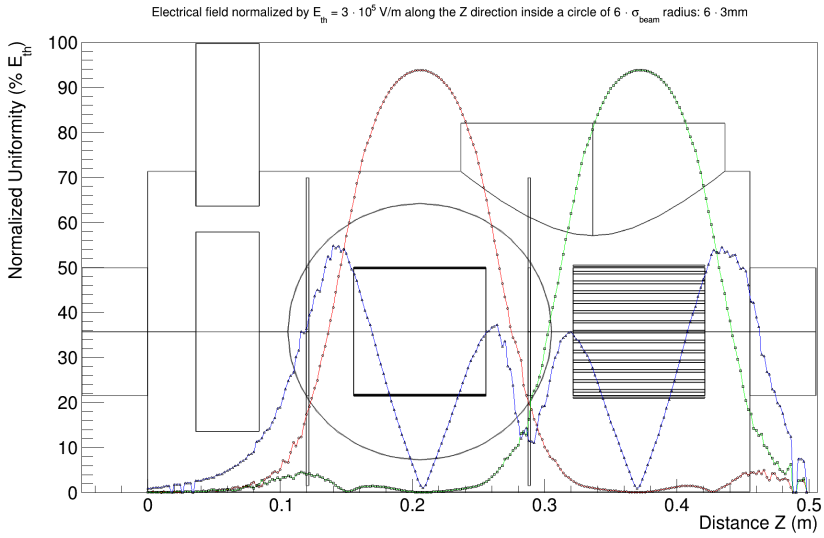

(a) Electrical field component in the LWU. The normalized average of the electrical field $\frac{\|E\|}{E_{extraction}}$ is calculated for each field direction (E_x in green, E_y in red, E_z in blue) along the LWU.

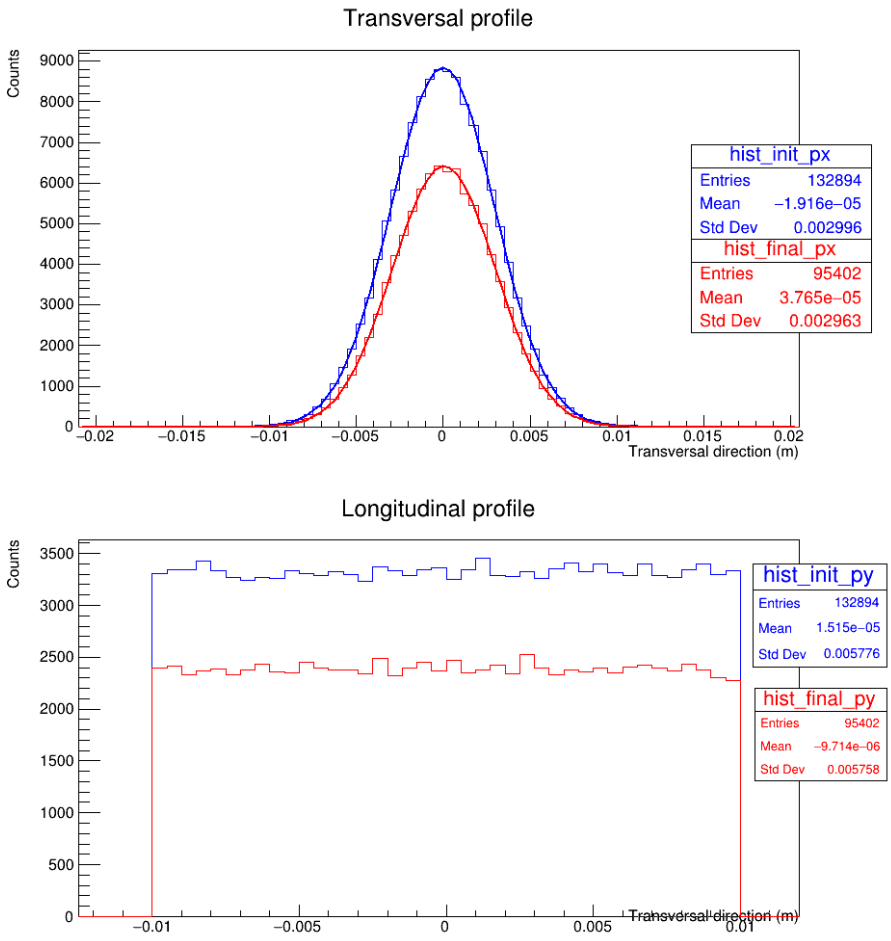

(b) Particles tracking. Initial ion distribution is plotted in blue. Red curve shows the ion distribution on the readout plane.

Figure D.2: Electrical field in asymmetric configuration.

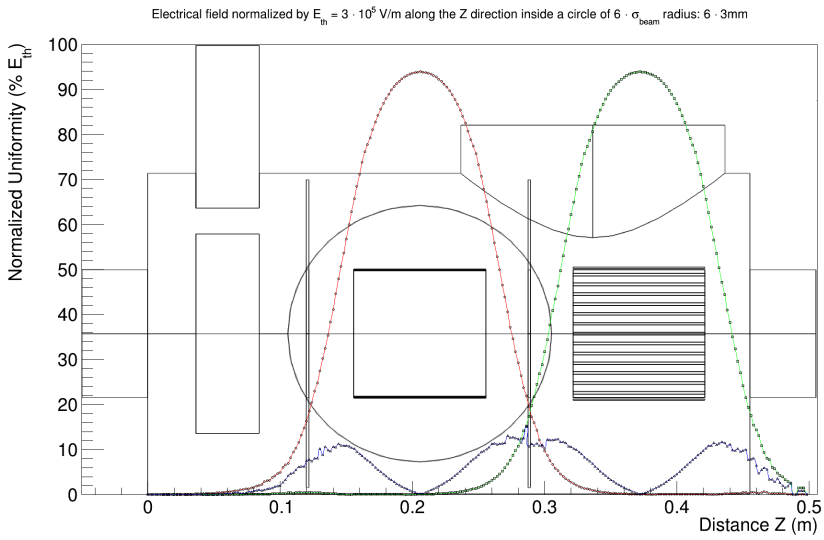

(a) Electrical field component in the LWU. The normalized average of the electrical field $\frac{\|E\|}{E_{extraction}}$ is calculated for each field direction (E_x in green, E_y in red, E_z in blue) along the LWU

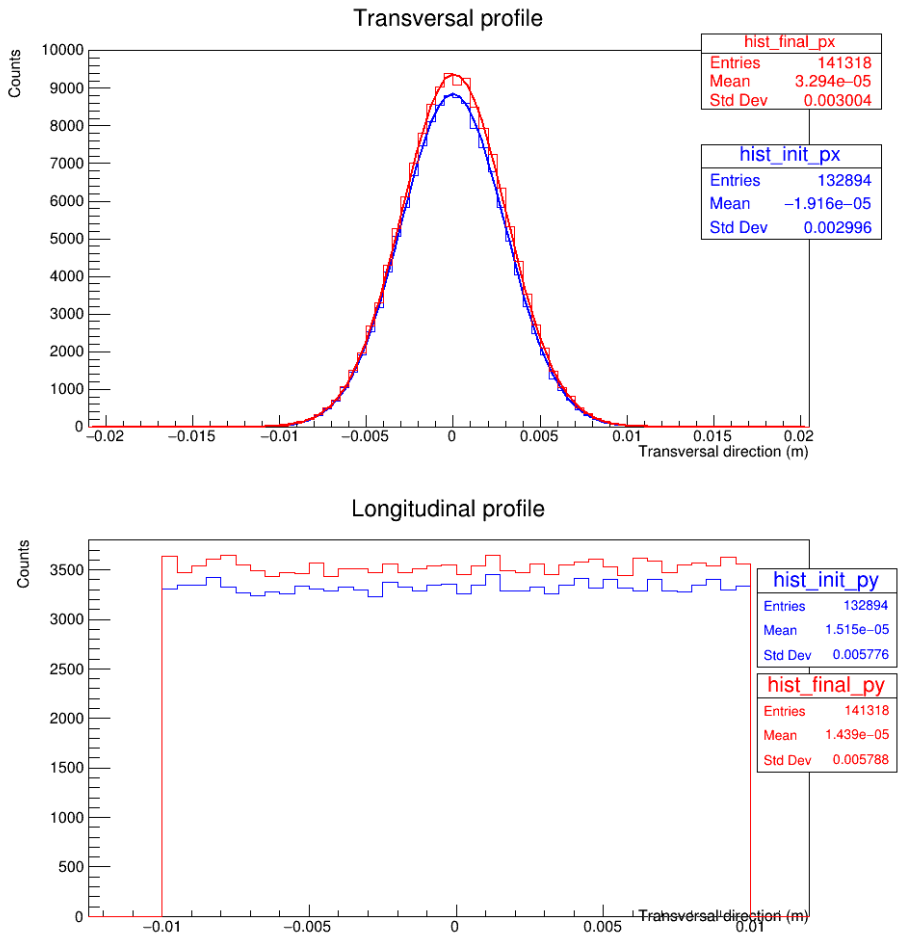

(b) Particles tracking. Initial ion distribution is plotted in blue. Red curve shows the ion distribution on the readout plane.

Figure D.3: Electrical field in symmetric configuration.

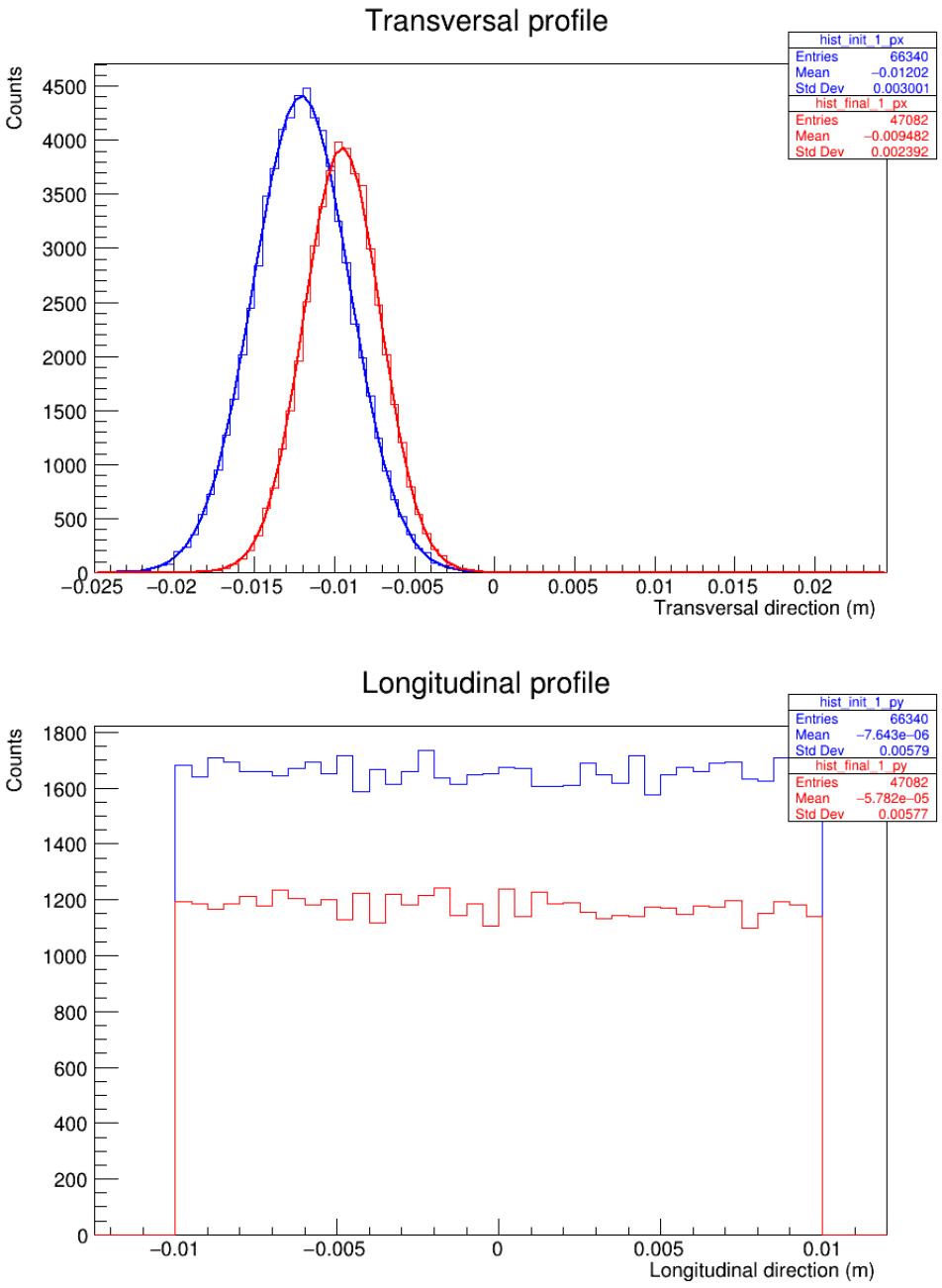

Figure D.4: Results from particle tracking in case of a symmetric IPM is used in asymmetric configuration. Initial ion distribution is plotted in blue. Red curve shows the ion distribution on the readout plane.

The optical IPM can work in symmetric and asymmetric mode. However, the field degraders have been optimized for a symmetric usage. If this IPM is used in asymmetric mode, then the extraction field will afflict the profile measurement. These effects can be simulated by COMSOL. The extraction field focuses particles and pull them in the center of the IPM.

Bibliography

[1] Hamamatsu. *MicroChannel Plate and MicroChannel Plate assembly*. Ed. by Hamamatsu. Dec. 10, 2018. URL: https://www.hamamatsu.com/eu/en/product/optical-sensors/electron_ion-sensor/mcp/index.html.

[2] EMVA. "Emva Standard 1288 Release 3.0". In: (2010). URL: https://www.emva.org/wp-content/uploads/EMVA1288-3.0.pdf.

[3] EPICS Collaboration. *EPICS, a set of Open Source software tools, libraries and applications developed collaboratively and used worldwide to create distributed soft real-time control systems for scientific instruments such as a particle accelerators, telescopes and other large scientific experiments.* Nov. 22, 2018. URL: https://epics-controls.org/.

[4] Mark Rivers. *asynDriver, a general purpose facility for interfacing device specific code to low level communication drivers.* Nov. 22, 2018. URL: https://epics.anl.gov/modules/soft/asyn/.

[5] Dirk Zimoch. *StreamDevice, a generic EPICS device support for devices with a "byte stream" based communication interface.* Nov. 22, 2018. URL: https://paulscherrerinstitute.github.io/StreamDevice/.

[6] Mark Rivers. *areaDetector, an application for controlling area (2-D) detectors, including CCDs, pixel array detectors, and online imaging plates.* Nov. 22, 2018. URL: http://cars9.uchicago.edu/software/epics/areaDetector.html.

[7] Murali Shankar. *https://slacmshankar.github.io/epicsarchiver_docs/index.html*. Ed. by an implementation of an archiver for EPICS control systems that aims to archive millions of PVs. EPICS Archiver Appliance. Nov. 22, 2018. URL: https://slacmshankar.github.io/epicsarchiver_docs/index.html.

[8] *The FASTER electronics*. URL: http://faster.in2p3.fr/.

[9] *DDC316*. URL: http://www.ti.com/product/DDC316.

[10] *Status report on the saclay high-intensity proton injector project (IPHI)*. (Vienna, Austria). JACoW Publishing, 2000. URL: http://accelconf.web.cern.ch/Accelconf/e00/PAPERS/THOAF202.pdf.

[11] Raphael Gobin et al. "High Intensity Beam Production at CEA/Saclay For The IPHI Project". en-us. In: *Proceedings of the 22nd Int. Workshop on ECR Ion Sources* ECRIS2016 (2016), Korea–. DOI: 10.18429/jacow-ecris2016-wepp01.

[12] F. Senée et al. "Increase of IPHI Beam Power at CEA Saclay". In: *Proc. 9th International Particle Accelerator Conference (IPAC'18), Vancouver, BC, Canada, April 29-May 4, 2018*. (Vancouver, BC, Canada). International Particle Accelerator Conference 9. https://doi.org/10.18429/JACoW-IPAC2018-TUPAF016. Geneva, Switzerland: JACoW Publishing, June 2018, pp. 694–696. ISBN: 978-3-95450-184-7. DOI: doi:10.18429/JACoW-IPAC2018-TUPAF016. URL: http://jacow.org/ipac2018/papers/tupaf016.pdf.

[13] Jan Egberts. "IFMIF-LIPAc Beam Diagnostics. Profiling and Loss Monitoring Systems". 2012PA112194. PhD thesis. 2012. URL: http://www.theses.fr/2012PA112194/document.

[14] Joseph Ladislas Wiza. "Microchannel plate detectors". In: *Nuclear Instruments and Methods* 162.1-3 (June 1979), pp. 587–601. DOI: 10.1016/0029-554x(79)90734-1.

[15] K. Baraka et al. *Garfield++ – simulation of tracking detectors*. URL: http://garfieldpp.web.cern.ch/garfieldpp.

[16] Wanzenberg. DESY, Hamburg, Germany, Internal Rep., DESY M 10-01. May 2010.